SANDCAM AT REHOBOTH:

QUANTIFYING SHORELINE CHANGE USING VIDEO

BY

NATHANIEL S. PEARRE

AND

JACK A. PULEO

RESEARCH REPORT NO. CACR-07-04
DECEMBER, 2007

CENTER FOR APPLIED COASTAL RESEARCH

OCEAN ENGINEERING LABORATORTY
UNIVERSITY OF DELAWARE
NEWARK, DE 19716

This work was supported financially by the Delaware Department of Natural Resources and Environmental Control and by the University of Delaware. We are grateful to the Henlopen Hotel for allowing us to deploy the cameras on their rooftop and supplying power and space for our equipment.

TABLE OF CONTENTS

LIST OF FIGURES

LIST OF TABLES

ABSTRACT

In this study we describe a video system deployed at Rehoboth Beach on the Atlantic coast of Delaware to monitor and quantify the evolution of a nourished beach. Hourly time exposure and variance images from seven (7) cameras are geo-rectified to a horizontal plane at the tidal elevation in a local coordinate system. Shorelines along 6 km of beach are automatically identified using pixel intensity gradients from the time exposure and variance imagery. Correlations between automatically identified and user-defined shorelines from images with various wave and atmospheric conditions exceed r^2 values of 0.92. Small variations in camera azimuth and tilt are found to significantly affect apparent shoreline locations and are automatically corrected through image correlation procedures. Hourly shoreline data are tidally and seasonally-averaged to quantify seasonal morphodynamic variability. Over a year and a half monitoring period the shoreline exhibits erosional and accretional variations of ~10 m that are highly dependent in the alongshore on permanent man-made structures and subject to seasonally characteristic littoral transport variations. Comparison of mean summer shoreline locations reveals an average erosion of ~0.3 m between the summer of 2006 and the summer of 2007, consistent with previous studies of this area. The temporal history of the planform area, obtained from shoreline position, showed weak correlation with

volume measurements and thus cannot be used as a proxy for volumetric nourishment performance at this site.

Chapter 1

INTRODUCTION

With each passing year the world's shorelines become more valuable and more densely populated. Commerce and industry compete for access to the water with recreational beachgoers and those who simply wish to live at the edge of the ocean. At the same time our growing understanding of the coast's importance to diverse ecologies demands that some areas be kept off limits to development. With the increased personal mobility and wealth of the American populous, development of communities on or near the water have skyrocketed throughout the last century. With that boom the demand for, and cost of real estate has soared. For the towns and municipalities that boarder the sea, the beach area can be an immense economic boon, attracting swimmers, sun-bathers, fishermen, and those who simply want to escape the world and be subsumed by the thunder of the surf. For whatever reasons people come to the beach, they spend the money which in many cases forms the backbone of the local economy. In addition, the beach serves as a vital physical barrier between the sea and developed areas, buffering against the potential destructive power of storm induced erosion. With so much at stake, monitoring the shoreline and understanding nearshore dynamics has become very important to the communities and all levels of government.

1.1 Background

Many scientific experiments designed to study the dynamic interaction of land and sea are based on the deployment of sensors in cross-shore and/or alongshore arrays to collect data on waves, currents, sediment transport and morphological evolution. While in situ sensors are both necessary and beneficial, they are of necessity sparsely deployed. To supplement in situ data, remote sensing techniques such as radar (e.g. Frasier, et al., 1995; McNinch, 2007), LIDAR (Stockdon et al., 2002; Robertson et al., 2004), and video (e.g. Holland et al., 1997 among many others) have also been used. Perhaps the most widely used of these techniques thus far is video-based remote sensing. The popularity of video is due both to the relative ease of deployment and to its low cost compared to the other approaches.

There are numerous video-based nearshore systems in use around the world and they are finding application in a great variety of roles in engineering, science and coastal zone management. Data from video systems have thus far been used to determine intertidal beach slope (e.g. Aarninkhof and Roelvink, 1999; Madsen and Plant, 2001), nearshore bathymetry (e.g. Stockdon and Holman, 2000; Holland, 2001), surface currents (e.g. Holland, et al., 2001; Chickadel, et al., 2003; Puleo, et al., 2003), wave period and direction (e.g. Lippmann and Holman, 1991), beach morphology (e.g. Holland and Holman, 1997; Holland and Puleo, 2001), rip current dynamics (e.g. Turner et al., 2007), as a tool tailored to coastal management (e.g. Davidson et al., 2007), and to estimate shoreline and sandbar locations (Lippmann and Holman, 1989; van Enckevort and Ruessink, 2001 and 2003; Aarninkhoff, 2003; Aarninkhoff et al., 2003; Boak and Turner,

2005; Plant et al., 2007). Among the data available through video, shoreline position is of value to coastal zone management because temporal variability in shoreline position quantifies beach planform variations (Farris and List, 2007) and can indicate erosion/accretion patterns. Shoreline location is a measurement particularly well-suited to video-based remote sensing because it can be extracted directly by a variety of methods suited to different conditions (e.g. Boak and Turner, 2005; Plant et al., 2007).

1.2 Objectives & Scope

The objective of this project may be summed up as an effort to further the development of visible-spectrum video for use in nearshore science, engineering and management. This objective requires two elements: The first is that a SANDCam (Surf And Nearshore Dynamics Camera) site must be established at Rehoboth Beach Delaware, including the setup and surveying of a system of cameras and the development of software for the extraction of shorelines from video data. The second is analysis of the dataset, which includes both the development of numerical tools to condense and synthesize the shoreline information gathered and the interpretation of that information in how it relates to periodic and evolutionary variability of the shoreline.

The most important tools presented intact at the outset of this project include programs and methodologies for the determination of camera lens distortions and for the transformation between 3-dimensional (3-D) real world coordinates and 2-dimensional (2-D) image coordinates developed by the Coastal Imaging Lab at Oregon State University. The hardware and software associated with image capture and transmission

was provided by Erdman Video Systems. To complete the intended analysis a host of functions were written to organize, process, display, archive, extract, and analyze the image data.

We report here on an effort to further automate the application of video systems in science and coastal zone management. Apparati and techniques have been developed to monitor and quantify the seasonal, episodic, and progressive shoreline changes occurring on 6 km of the Delaware coast in a fully automated fashion in near real-time. The wave characteristics and littoral transport of the study area are discussed in Chapter 1.3. Chapter 2 describes the imaging system, including finding lens distortion (2.1), the apparatus and procedures of the field site system setup (2.2), the site survey procedure (2.3), as well as how multiple oblique camera images are transformed into a single merged planform images (2.4). Chapter 3 describes types of images recorded and how they are used to find quantitative shoreline data, including the method used to correct for camera movement. In Chapter 4 the automated quality control and data vetting metrics are discussed. The results of almost a year and a half of data are presented in Chapter 5 and indicate an average summer 2006 to summer 2007 shoreline recession of ~0.3 m, though dramatic changes in shoreline position (~10 m) are found on weekly timescales. Chapter 6 presents a discussion of the relationship between beach planform area and sediment volume (6.1), errors in the assumed vertical position of the shoreline (6.2), possible causes of camera movement (6.3).

1.3 Site Information

Delaware is located on a peninsula between the Delaware and Chesapeake Bays with water frontage on the Delaware Bay and the Atlantic Ocean. The Atlantic coast of Delaware consists of roughly 30 km of sandy beach (Figure 1.1C and 1.1D). Twenty-year mean offshore wave heights are 1 m or less with mean significant periods of 6-7 seconds (Bosma and Dalrymple, 1997). Wave heights exceeding 3 m are rare but heights over 7 m can occur during severe storm events. Concurrent wave information applied to this study is from NOAA-NDBC Buoy 44009 located approximately 45 km to the South-East of Rehoboth Beach in 28 m of water. Tide along the Delaware coast is semi-diurnal with a mean range of 1 m and a standard deviation of 0.25 m.

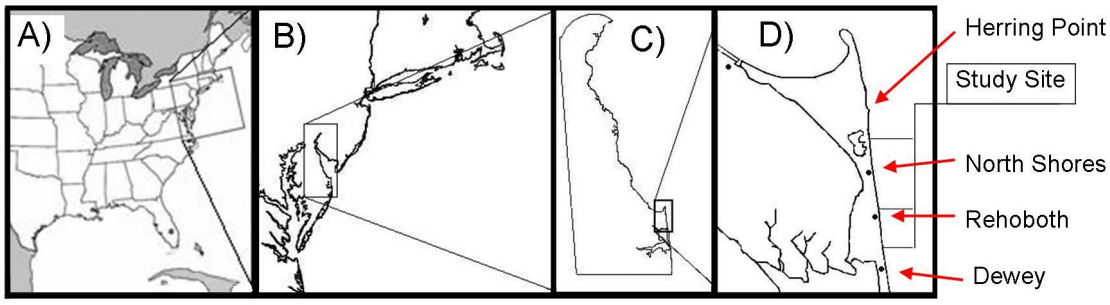

Figure 1.1: A nested map of the study site including A) the United States, B) the central portion of the Eastern Seaboard C) the state of Delaware, bounded in the east by the Delaware bay and the Atlantic Ocean, and D) the northern part of Delaware's Atlantic coast. The study site includes the town of Rehoboth Beach and the private community of North Shores. The three lines labeled "Study Site" represent the northern edge of the site, the location of the cameras and the southern edge of the site respectively, representing a distance of 6 km.

The Atlantic coast of Delaware experiences a unique littoral transport scheme due to varying seasonal wave conditions and large-scale landforms. Wave energy from the north is reduced along the northern Delaware beaches by the coastal geometry of New Jersey (Figure 1.1B). Wave energy from the south has an effectively infinite fetch and is unencumbered. This variation in the directional distribution of wave energy is a function of location on the coast, such that the wave directional spectrum is much more strongly biased to wave energy from the south in the northern sections of the state, tapering to almost no bias near the Maryland-Delaware border. The result of this spatial variation in the directional spectrum is a divergence zone (nodal point) in the net littoral transport along the coast, also roughly at the Maryland-Delaware boarder (Dalrymple and Mann, 1985). North of this nodal point, net littoral transport is to the north while south of this point net littoral transport is to the south. Estimated net littoral transport rates north of the nodal point are on the order of 117,000 m^3/ year (Dalrymple and Mann, 1985).

These large transport rates result in the continued growth of Cape Henlopen at the mouth of Delaware Bay at more than 5 m/year (Honeycutt, 2003). Without any other sediment source such as significant river discharge or erodable headlands, the material deposited at Cape Henlopen implies erosion along the length of Delaware coast. Estimates for the natural (unencumbered) rate of erosion vary from 0.5 m/ per year near the nodal point (Dalrymple and Mann, 1985) to 2 m per year near the northern end of the littoral system (Garriga and Dalrymple, 2002; Honeycutt, 2003) with considerable spatial variation along the intervening span.

This littoral drift scheme is complicated by the effects of a sand bypassing pump at the Indian River inlet, roughly 10 km south of the southern edge of the study site, which provides on average 70,000 m^3 of sediment to the northern side of the inlet (standard deviation over 10 years of bypassing is 15,000 m^3). Pumping operations vary on monthly timescales due to operation limited to, on average, 6.5 days per month (Clausner et al, 1992) and on yearly timescales due to efforts to minimize disruption to recreational beach use in the summer months (Garriga and Dalrymple, 2002). Additional complexity arises from the construction of a 91 m long shore normal stone groin at Herring point 1.5 km to the North of the northern edge of the study site (Figure 1.1D). A wood and stone groin was built in the 1950's at the same location to protect the Herring Point gun battery, a part of Fort Miles (now a national historic site), located on a bluff behind the beach. These groins were in very poor condition, allowing significant bypassing landward of their original extents. The reconstruction was predicted to accumulate 55,000 m^3 of sediment, or roughly half of the mean yearly alongshore drift at that location, on its updrift (southern) side (DNREC, 2007). Construction of the new groin was completed in early May 2007, and the effect on the shoreline locally was immediate and dramatic; The beach on the southern side of the groin accreted to within a few meters of the end of the groin by the end of July 2007.

Figure 1.1D shows the roughly 6 km study area consisting of Rehoboth Beach (public), the community of North Shores (private) and state parkland near Herring Point. The shoreline along this section is occasionally punctuated by shore-normal groins. Due to the high erosion along this section of coastline, Delaware's Department of Natural

Resources and Environmental Control (DNREC) and the U.S. Army Corps of Engineers (USACE) have performed beach nourishment projects with the most recent occurring in 2005. A 4 km stretch from Dewey Beach to Rehoboth Beach (refer to Figure 1.1D) was widened 38 m at a cost of $10.3 million as the first step of a beach maintenance plan that will include re-nourishments every 3 years or as necessary (U.S. Army Corps of Engineers, 1997). Due to high mobilization and nourishment costs, there is great interest in quantifying the project performance as well as in monitoring the site to identify and characterize possible problematic locations.

Traditional beach surveys are undertaken by DNREC but are coarsely sampled in space (every 150 – 300 m along the beach) and time (once or twice per year). To capture small-scale, high-frequency variations, shoreline variability is investigated through video-based remote sensing. We note that the methods described herein cannot be used to quantify three-dimensional beach variability and thus serve as a complimentary measurement to standard surveying procedures when sediment volume is the primary focus. Comparisons between planform area determined from shoreline position and beach volume from a complimentary LIDAR study will be discussed in Chapter 6.1.

Chapter 2.

THE IMAGING SYSTEM

This chapter describes the apparatus used in this study, consisting primarily of a system of video cameras that capture images of the beach. Details of the interrelationship between the cameras and how oblique images are mapped onto a grid of the study site to be displayed as a geo-normal view are discussed in Chapters 2.2 through 2.4, but first it is necessary to gain some understanding of the relationship between the 3-D world and the 2-D image captured by a camera.

2.1 Lens Calibration

The world about which we wish to know lies at some distance from an array of cameras. Light making up an image of the world passes through a camera lens and is focused on the imaging hardware of the camera. Digital cameras convert the incoming light into an electrical signal on a charge-coupled device (CCD). The ideal (undistorted) image produced by a camera-lens combination can be modeled as that produced by an ideal pin-hole camera with the image defined by the size of the camera's CCD located one focal length from a virtual camera center point. To simplify the analogy, the plane of the camera image can be imagined in front of the camera's virtual center so that the image appears in the correct orientation in front of the camera, rather than inverted and behind it as would be the case with an actual pin-hole camera. A lens with a short focal length

puts the image plane close to the camera's virtual center, so a wider slice of the real world is imaged, while a lens with a longer focal length reduces the angle that can be seen. Figure 2.1 provides a depiction of this conceptual relationship between the image plane, the lens focal length and the size of the camera's CCD.

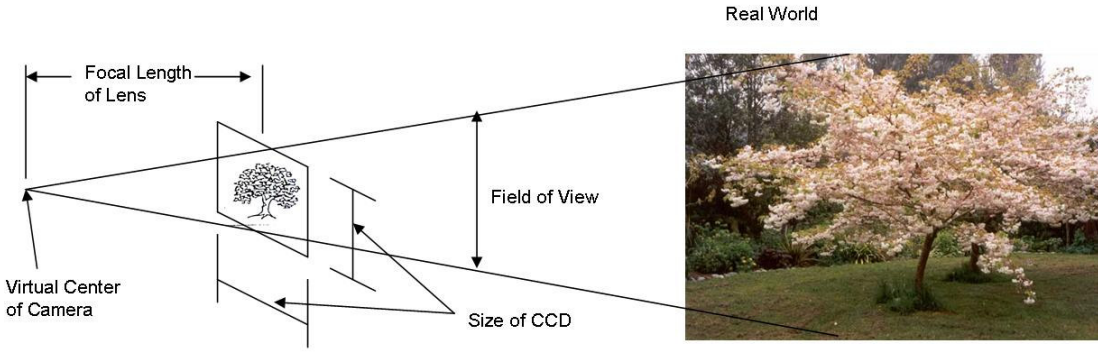

Figure 2.1: Depiction of the pinhole camera analogy for the image plane and focal length of a camera.

The image that results from most lenses is distorted relative to the ideal image produced by the methodology described above. The pattern of distortion mirrors the way a human eye behaves. With a high spatial density of optical cones near the center of the retina we have amazingly sensitive vision in the direction we are looking. Cone density decreases with distance from the center of the retina, but continues to provide some sensitivity at large angles (in some individuals as far as 90°) from center. To mimic this, short focal

length (wide angle) lenses push the center of the image apart to provide greater detail in the area of interest and pull the image together at the periphery to maximize field of view. This pattern of distortion can be modeled as a radial pixel displacement proportional to a cubic function of the distance from the image center (Karara and Abdel-Aziz, 1974; Tsai, 1987). Figure 2.2A shows the image produced by a 3.5mm lens of a regular orthogonal pattern of white dots. In Figure 2.2B the location of each dot in the image (plus signs) is shown with a best fit interpretation of where the dots would appear if no lens distortion were present (open circles).

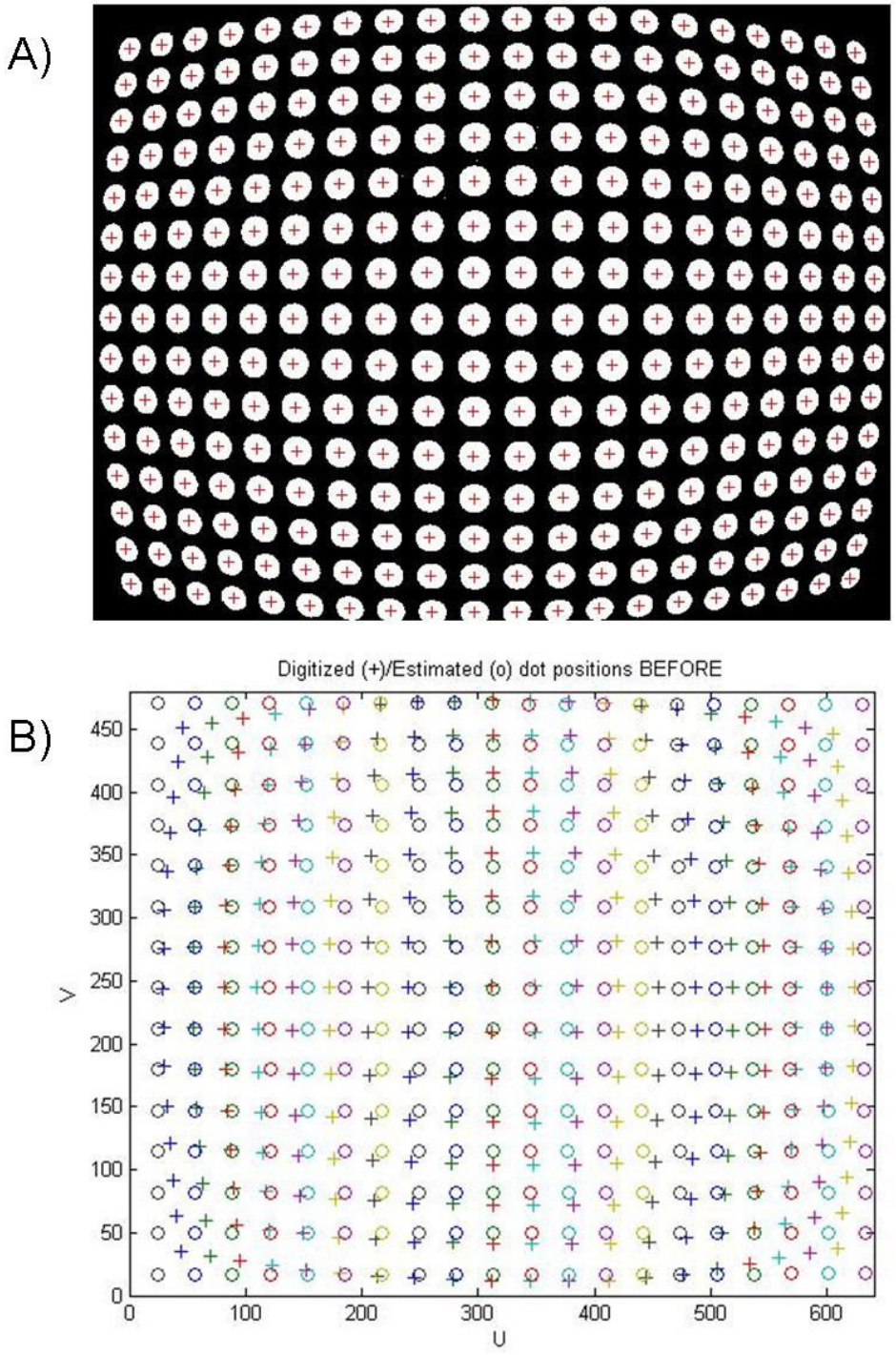

Figure 2.2: A calibration image for the 3.5mm lens used on the offshore-looking camera. A) The raw image including the dot mass centers. B) Dot centers (pluses) superimposed on regular orthogonal grid (circles).

Using the dot location errors obtained in Figure 2.2B, the radial displacements of each dot can be mapped as a function of distance from the center point of the distortion. The center of distortion is not necessarily located at the center of the image, but the two are usually not far apart. The distortion center is located by the best fit of dot locations established in Figure 2.2B. Figure 2.3A is a map of total pixel displacement as a function of image location. The displacements are exaggerated and indicated with a blue arrow. Note how pixels near the center of the image are displaced outwards, effectively magnifying anything that appears in the center of the screen. At the periphery of the image pixels are displaced towards the center, increasing the total field of view though at lower resolution. In Figure 2.3B the radial component of the displacement is quantified as a function of radial distance from the distortion center. To these data a cubic polynomial is fitted

$$\Delta = D_1 r + D_3 r^3, \qquad (1)$$

where Δ is the radial displacement, r is the radial distance from the distortion center, and D_1 and D_3 are the distortion coefficients. Figure 2.3C shows the residual errors remaining once the correction (Equation 1) is applied to the total error from this 3.5 mm lens. While the residual errors may appear to exhibit patterns, they should not be radially dependent, and could not be accounted for without the development of much more complex formulas.

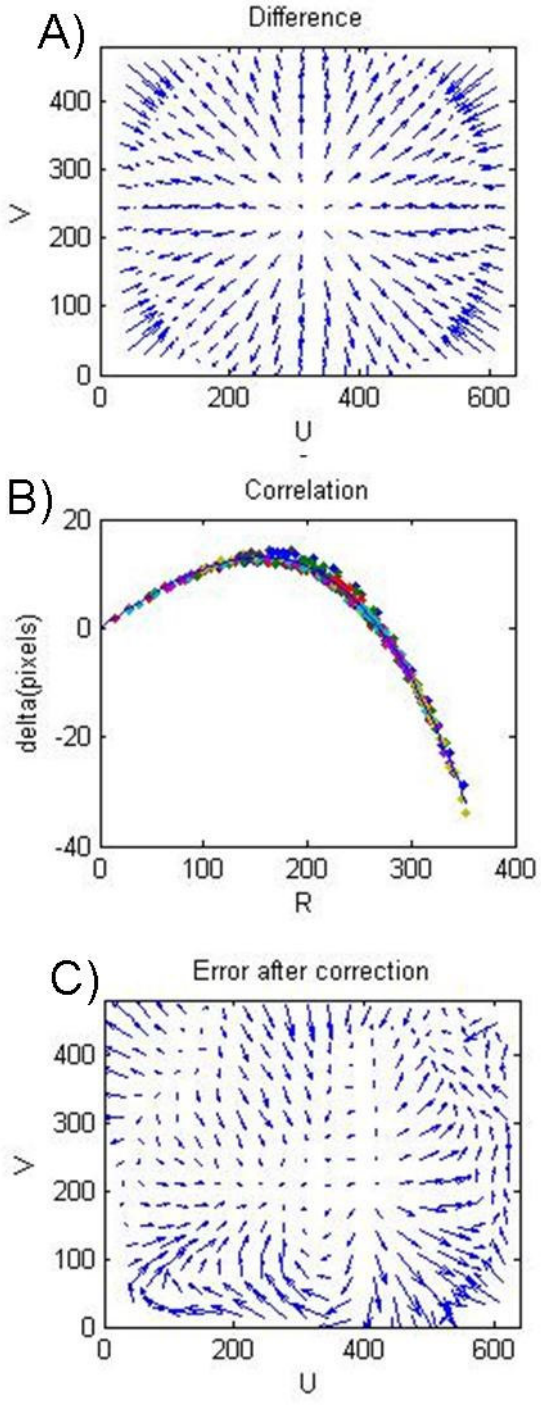

Figure 2.3: Parameters output from the lens calibration define the pixel displacement as a function of distance from image center.

In this project lenses with focal lengths ranging from 3.5 mm to 50 mm were used. For each of the lenses tested, Table 2.1 provides the D_1 and D_3 coefficients used in Equation 1 and the distortion center [U_o V_o] as determined by the best-fit algorithm. It should be noted that convention places the origin of an image in the upper right corner, which results in all pixel locations being positive in the horizontal (U) direction and negative in the vertical (V) direction. The distortion center values refer to camera CCDs with 640 x 480 pixels, so the true image center in all cases would be U_o = 320, V_o = -240. The sixth and seventh columns list the standard deviation (σ) of radial pixel displacements and of radial errors remaining after correction (circumferential errors are not accounted for). The final column in Table 2.1 is the horizontal field of view in degrees of each of the lenses, which can be seen to correspond to focal lengths as indicated in Figure 2.1.

Table 2.1: Lens distortion parameters for lenses used in this experiment (and alternates).

Focal Length	D1	D3	Uo	Vo	Distortion	Error after Correction	Field of View
(mm)			(pixels)	(pixels)	(pixels)	(pixels)	(degrees)
3.5	-1.74E-06	0.12578	320.5	-235.2	10.37	0.794	88.4
6	-4.22E-07	0.03079	323.3	-242.9	2.80	0.294	54.9
9	-2.94E-07	0.02059	319.9	-242.8	1.93	0.177	37.9
12	-3.06E-07	0.02211	319.5	-238.2	2.05	0.174	29.2
25	2.49E-09	0.00027	306.5	-399.5	0.156	0.124	14.2
35	-1.01E-08	0.000755	336.1	-254.2	0.131	0.118	10.3
50	-4.56E-09	0.00034	346.6	-276.8	0.100	0.076	7.0

2.2 Imaging System Setup

The spatial resolution and viewing distance of any imaging system depends on the imaging equipment and the elevation at which it is deployed. The system described here was deployed on the roof of the Henlopen Hotel at roughly 30 m above mean sea level at the end of March, 2006. Image collection for analysis began at the end of April, 2006. Because of the exposed rooftop location, an effort was made to insure the stability of the camera mounting structure and to insulate the structure from the elements. A stable base for the camera mounts and associated hardware is provided by heavily weighted wooden palettes measuring approximately 1.2 m square. Two palettes, constructed of a pressure treated 4x4 frame (0.089 x 0.089 m members) and ¾" (0.019 m) thick marine grade plywood are placed on the northeastern and southeastern corners of the roof (Figure 2.4). During construction of the palettes each piece of wood was primed with exterior latex primer before assembly. The assembled palette was then coated with exterior grade oil-

based paint in an effort to minimize moisture intrusion. The palettes are stabilized with roughly 20 kg of lead weight enclosed within the frame and 160 kg of sandbags resting on top of the pallets between the cameras and other hardware.

Figure 2.4. Four of the seven cameras (cameras 4, 5, 6, & 7) are mounted on a palette on the North-East corner of the hotel roof. Note sandbags for stability, static dissipation tower with copper grounding cable, and weatherproof camera housings with bird deterrent spikes. The second (gray) cable is an emergency tether to keep the palette from falling if it is dislodged during extreme wind events.

Seven Panasonic video cameras (model: WV-CL920A; ½"CCD, 640 x 480 pixel resolution) are distributed on the two palettes. The cameras are numbered 1 through 7 according to aim; camera 1 facing almost due south and camera 7 facing almost due

north. Cameras 1 through 5 are arrayed such that their fields of view overlap to cover over 180° of beach from the southern to the northern horizon. Cameras 6 and 7 are equipped with zoom lenses and are positioned to provide higher resolution imagery of the area of shoreline in and around the groin field at North Shores approximately 2000 m to the north of the hotel (see Figure 1.1D). To maximize resolution, lenses of different focal length are used. On the principle 5 cameras, 12 mm focal length lenses are used on the two flanking cameras aimed north and south (cameras 1 and 5), a 3.6 mm lens is used on the offshore facing camera (camera 3) and 9mm lenses are used on the two cameras aimed in between (cameras 2 and 4, similar to Aarninkhof and Holman, 1999, except here the offshore facing camera used a 3.6 mm lens). Cameras 6 and 7 are equipped with a 25 mm and a 50 mm lens respectively (see Figure 2.5A for details on camera aim and pixel footprint resolution). Cameras are protected by Pelco environmental enclosures on pedestal mounts roughly 0.5 m above the surface of the pallets. The aluminum pedestals are through-bolted to the pallets, which are protected from crushing by additional pressure treated 4x4 reinforcements.

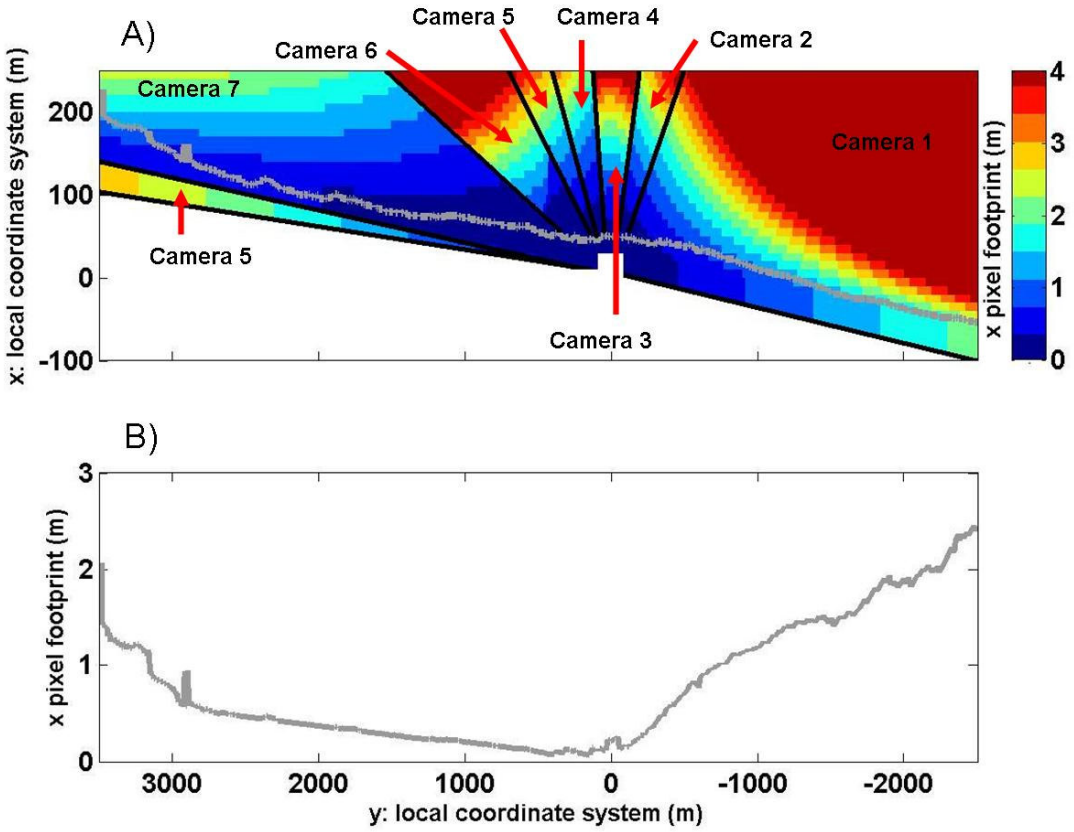

Figure 2.5. (A) The cross-shore pixel footprint for the 7 cameras displayed on the local coordinate system grid. Note that Cameras 5 is a wider angle lens that spans the field of view of both cameras 6 and 7. (B) Expected pixel footprint along a typical mid-tide shoreline.

It should be noted that the initial intended camera/lens configuration was to have been, from south to north (camera 1 through camera 7); 12mm – 9mm – 6mm – 9mm – 12mm 35mm – 50mm. Upon review of the camera geometries and the merged planform image (Chapter 2.4) it was discovered that this configuration failed to provide adequate total field of view to cover the entire beach while maintaining the overlaps between each

camera necessary both for geometry verification and to smooth the merged planform image. We speculate that this was due to the proximity of the hotel to the swash zone (roughly 70m) compared to previous applications where a smaller span of beach was imaged and the cameras were sited further back from the shore. By replacing the 6mm lens in camera 3 with a 3.5 mm lens, the field of view was increased from ~55° to ~88.5°. Figure 2.5B depicts the cross-shore pixel footprint, which defines the maximum possible resolution, as a function of longshore location within the study area. From this graph it is clear that despite the reduced resolution of camera 3 caused by using a wide-angle (3.5 mm) lens, the cross-shore pixel footprint size, and hence the spatial resolution in the area immediately in front of the hotel, is still among the best in the study area.

The cameras from each pallet are connected to a sampling computer (Erdman Video Systems) that controls the temporal sample spacing and imagery collection type (see Chapter 3.1). Raw imagery is collected every hour from 7 am to 6 pm over the course of the hour. Data is collected from each camera for 10 minutes. Because information from only one camera can be collected at a time on each of the two computers, each hour's data collection spans roughly 40 minutes. When all image types have been collected for each of the seven cameras a data packet is sent via FTP to the University of Delaware for archiving, automated processing and web dissemination (http://sandcam.coastal.udel.edu). Figure 2.6 is a graphical depiction of the data path.

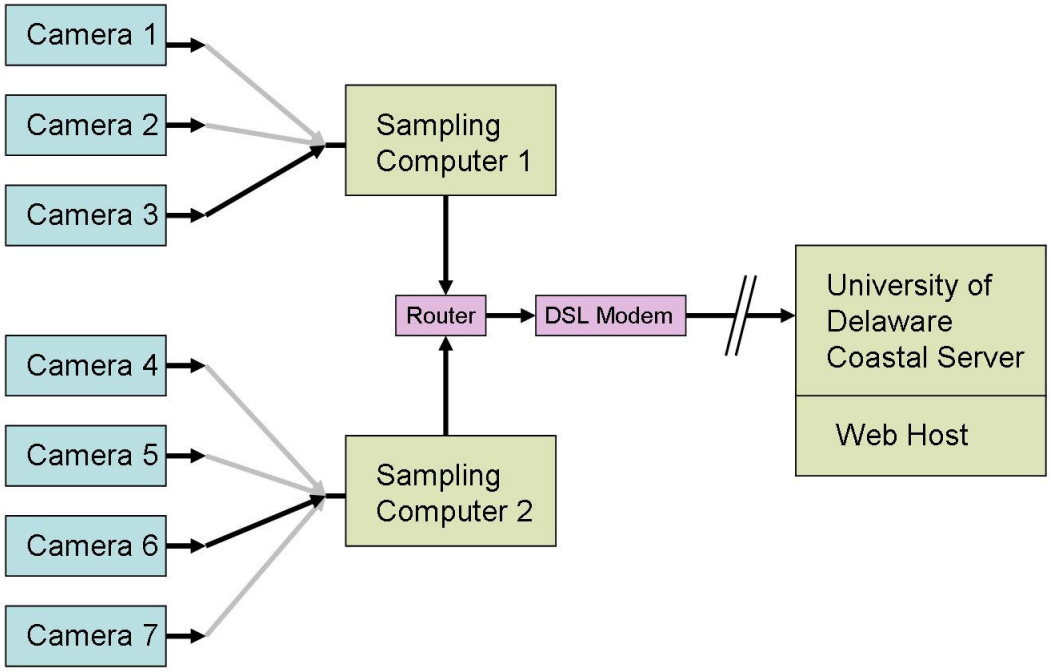

Figure 2.6: The data path from cameras to web-site. Each of two Erdman sampling computers collects data from each of a subset of the cameras. Cameras are sampled sequentially during each hour, collection takes ten minutes for each of the cameras. At the end of collection that hour's data packet is FTP'd to the University of Delaware coastal server for automated processing and web dissemination.

2.3 Site Survey

In order for quantitative information to be extracted from the oblique images captured by the cameras, they are first cast into a local coordinate system designed around the physical area of the study site. The local coordinate system at Rehoboth Beach is defined with axes parallel with and perpendicular to the edge of the boardwalk in front of the Henlopen Hotel such that *Y* is positive to the north and *X* is positive offshore. With this definition, the local coordinate system *Y* axis at Rehoboth Beach lies 0.17051 radians

(9.7695°) counterclockwise from True North (Delaware State Plane North). The local coordinate system origin is located at the head of a bolt attaching the 6x6 (0.14 x 0.14 m) boardwalk toe-rail, under the street light between the Henlopen Hotel and the Stuart Kingston Gallery.

In aiming the cameras, not only is it important that the entire shoreline in the study site be covered, but there must also be some overlap between the fields of view of adjacent cameras. It is also desirable (though not strictly necessary) that the fields of view of all cameras include the horizon. With the cameras affixed to the pallets on the roof of the hotel and the data and power cables attached to both cameras and the computers, the imaged field of view of each camera can be displayed and used to adjust the aim of each camera to insure that the above conditions are met.

The parameters used to define each camera's aim are referred to as a *geometry*. To establish a camera's geometry there must be a selection of identifiable fixed points of known location, called Ground Control Points (GCPs), within the field of view. Because three points in space define a plane, establishing the geometry of each camera can be done with a minimum of three GCPs, or two if the location of the camera itself is known. As additional points are included beyond this minimum, some degree of redundancy can be achieved, or the magnitude of errors in surveyed positions can be assessed from the redundant information. Because lens distortion residual errors (Figure 2.3C) vary over the image having GCPs distributed as widely as possible within the camera's field of

view is advantageous. Where no suitable fixed points exist on the beach, the use of supplemental man-made GCPs can improve this distribution.

Figure 2.7 shows time exposure images taken by each of the seven cameras during a site survey. (The image products recorded by the computers and used for shoreline quantification will be discussed in Chapter 3.1). Note the presence of wooden disks in each image painted black for visibility against the white sand. These disks, used as supplemental GCPs to improve the GCP distribution throughout the image, range in diameter from 0.6 to 2.4 m and are located on the beach to maximize the range of image locations where GCPs are present. These targets in addition to numerous fixed locations such as street lights and fence posts were surveyed by the Delaware Department of Natural Resources and Environmental Control in Delaware State Plane feet using a total station. The location of the glass plate of each camera housing (roughly 2-3 cm in front of the camera's focal plane) was also surveyed and used as a proxy for the camera's location. Survey data were converted into the local coordinate system for subsequent calculations. Camera geometries were determined for each camera following Holland et al., (1997) using user-chosen image coordinates (U, V) of a subset of the targets in each camera's field of view.

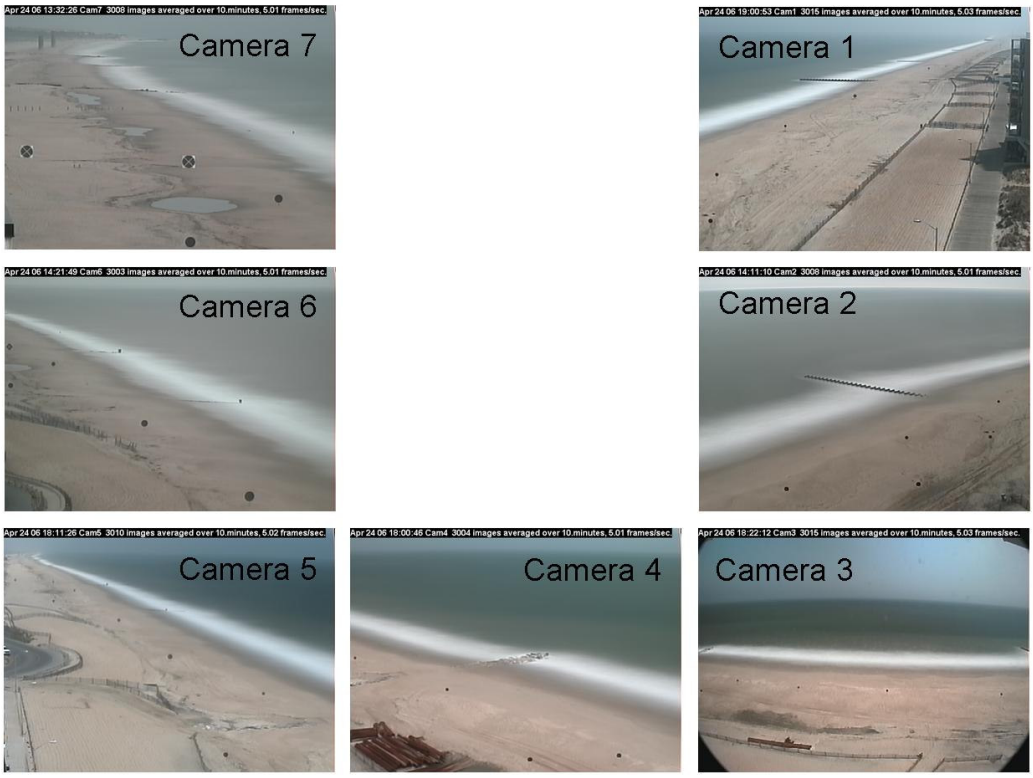

Figure 2.7: Images taken during the site survey. Black disks planted on the beach are wooden GCPs used in determining the geometrical transformation between world coordinates (*Xc*, *Yc*, *Zc*) and image coordinates for each camera (U*i*, V*i*).

2.4 Geo-rectification and Merge

From information acquired during the site survey we can determine the geometrical transformation allowing any 3-D coordinate in the scene *Xc*, *Yc*, *Zc* to be mapped into image coordinates for any camera *i* (U*i*, V*i*). Unfortunately the inverse transformation of determining the 3-D coordinates of an arbitrary pixel from a 2-D image is not possible with a single camera. Each pixel location on a camera image can be translated to any 3-D point on a ray that extends from the camera's virtual center out to infinity. To select which point along this ray to use, more information must be supplied. Because our

primary concern is determining shoreline position, the additional constraint imposed is that the pixel must lie on a horizontal plane defined by the tide level. Thus, the color information for each pixel is projected onto the point where the unique ray intersects the tide level. The resultant image produced for each of the seven cameras can be seen in Figure 2.8. Note that this transformation cannot account for vertical structures. Two World War II era submarine watch towers which can be seen in the upper left of the camera 7 image in Figure 2.7 can be seen in Figure 2.8 to have been 'smeared' into the horizontal tidal plane. The black area in the rectified image of each camera in Figure 2.8 is outside the field of view for that camera, so no data is present.

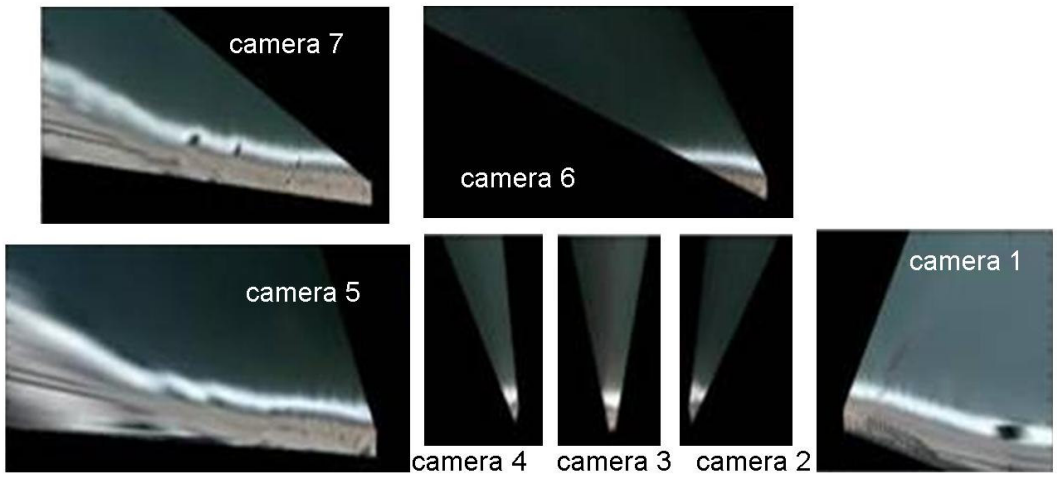

Figure 2.8: Images from each of the 7 cameras are rectified to a ground plane in the local coordinate system, defined as the level of the tide.

To assemble the seven camera images into a merged planform image of the study site, all images are geo-rectified to a common grid built on the local coordinate system described in Chapter 2.3. The grid points at Rehoboth used for generating merged planform images are defined by (*Xc*, *Yc*, *Zc*), where *Xc* extends from -100 to 400 at 1.5 m intervals, *Yc* extends from -2500 to 3500 at 6 m intervals and *Zc* is the tide level prediction obtained at the temporal mid-point of imagery collection. Tidal elevations are developed using the tidal harmonics package XTIDE (www.flaterco.com/xtide) for Ocean City, Maryland. The tidal lag between Ocean City and Rehoboth Beach is approximately 12 minutes. We view the time offset as negligible in our analysis since the imagery is collected over a 40 minute long time span.

Figure 2.9 shows a composite image obtained by merging the rectified images from the 7 cameras. Where rectified images overlap, merged planform image pixel intensity is determined as a weighted average of the pixel intensities provided by the two overlapping images. The weighting is a linear function of the ratio of the distances to the edges of each of the two images.

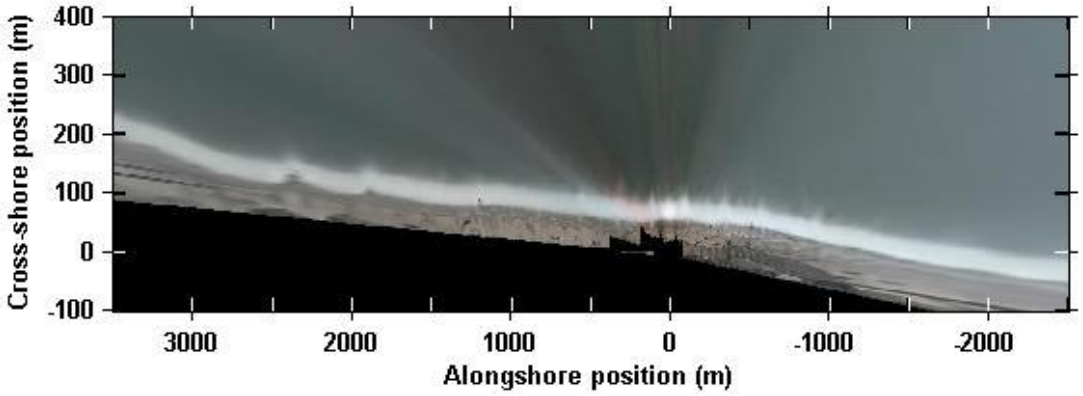

Figure 2.9. The merged planform time exposure image in a local coordinate system spanning 6000 m in the alongshore (with 6 m grid spacing) and 500 m in the cross-shore direction (with 1.5 m grid spacing). Areas of the grid not imaged by any of the cameras are mapped to black.

Chapter 3

SHORELINE QUANTIFICATION

In this chapter the image types, tools and algorithms needed to extract a quantitative shoreline position from camera imagery are described.

3.1 Image Types

Video imaging systems used for nearshore analysis generally collect three types of imagery: a snapshot, a time exposure image (referred to as timex) and a variance image (e.g. Holland et al., 1997; Aarninkhof and Holman, 1999). The snapshot (Figure 3.1A) is a single still frame from the scene of the camera providing visual identification of the nearshore conditions (e.g. large vs. small waves). The timex (Figure 3.1B) is a digital time exposure created by taking the average image intensity at each pixel over a ten minute time span (in this case 3000 images from a 5 Hz video signal). Individual wave features are de-emphasized in favor of average conditions, enabling a mean shoreline position to be isolated via gradients in pixel intensity. The variance image (Figure 3.1C) is obtained by taking the variability in image intensity for each pixel during the same 10 minute time span. Regions with high variability (near the surf zone) are mapped to white, while regions of low variability (the beach and offshore) are mapped to black. Persistent features such as the outer edge of the surf zone, indicated by a shoreward

transition from dark to bright pixel intensity, and the shoreline indicated by a shoreward transition from bright to dark pixel intensity can be seen.

Figure 3.1: The three types of recorded imagery. (A) Snapshot (B) Time exposure image consisting of averaged pixel intensity over 10 minutes. (C) Variance image showing the amount of change in pixel intensity over 10 minutes.

3.2 Compensation for Camera Movement

Despite efforts to stabilize the cameras and to isolate their mounting structures both from mechanical and environmental variability (described in Chapter 2.2), the cameras move slightly causing the apparent location of fixed objects to change over time (see Chapter 6.3). While such movements are likely to occur for all cameras and indeed all outdoor installations (Holman and Stanley, 2007), it is only for cameras that image distant objects that such movements have significant impact. In this study, cameras 1 and 7, with a 12 mm lens aimed south and a 50 mm lens aimed north respectively, were found to produce the least consistent rectified locations of fixed objects. While movements in camera 6, the north aiming camera with the 25 mm lens were also occasionally detected (and we

speculate are caused by the same angular displacement of the supporting structure), the alongshore extent that this camera covers is less than 500 m, much of which overlaps with the two adjacent cameras. Two factors contribute to the exaggerated presence of this problem in cameras 1 and 7: As the distance between camera and scene is reduced, the effect of angular camera movement is also reduced. In addition, shorter focal length (wider angle) lenses produce less image movement for a given camera movement, so movement in the remaining cameras is neglected.

To compensate for camera movement a procedure similar to particle image velocimetry (PIV; e.g. Adrian, 1991) was developed to identify changes in the azimuth and tilt directions. A region of interest (*ROI*) is chosen for an image from each camera to consist primarily of fixed objects with distinct patterns. For example in camera 7 the test region consists of fixed wooden pilings of 0.3 m diameter that appear dark against the bright sand beach background (visible in the middle of the left-hand edge of the camera 7 image in Figure 2.7). The sizes of the *ROI*s vary but are kept to roughly 5000 pixels to keep computation time manageable. An image from a survey date with known geometrical transformation (SURVEY), and the *ROI* of the test image (TEST) with unknown geometrical transformation are first converted to grayscale. Maximum expected movements are defined as 8 pixels in the vertical (tilt) and 4 in the horizontal (azimuthal) directions. For each possible position that TEST can occupy in SURVEY within the expected movement, an error correlation parameter $C_{\Delta Row,\Delta Column}$ is calculated (Roth et al., 1995; Hart,1998) as

$$C_{\Delta Row,\Delta Column} = 1 - \left(\frac{\sum \left| TEST_{i,j} - SURVEY_{i-\Delta Row, j-\Delta Column} \right|}{\sum TEST_{i,j} + SURVEY_{i-\Delta Row, j-\Delta Column}} \right), \quad (2)$$

where $TEST_{i,j}$ is the pixel in the i^{th} row and j^{th} column in the *ROI* of TEST, $SURVEY_{i-\Delta Row,j-\Delta Column}$ is the pixel at the corresponding (shifted by Δ_{Row} and Δ_{Column}) location in SURVEY , || denotes absolute value. The sub-pixel peak of the resulting image correlation matrix is determined using a 2D quadratic curve fit on the correlation peak and its 8 surrounding neighbors. The fitted peak provides the change in camera azimuth and tilt from the original known azimuth and tilt allowing new geometrical transformations to be calculated. In approximately 1 in 15 image sets no peak exists within the correlation matrix (*i.e.* the greatest correlation value occurs at the edge of the matrix). This is usually due to poor visibility (e.g. severely overcast or fog). In these cases, the most recent valid camera movement and corresponding geometrical transformation is used (up to 24 hours old). In rare circumstances (<0.5% of hourly images) no satisfactory transformation can be determined over the previous 24 hour period and the image rectification and subsequent shoreline determination are abandoned.

In order to test the procedure for determining camera movement, tilt and azimuth variations determined by eye were compared to those returned by the image correlation algorithm. Ten users were asked to compare an image with known geometrical transformation with 39 other images from the same camera spanning a month by locating the same feature in all images. Figure 3.2 shows the results of this comparison for the 50 mm lens (open circles) and the 12 mm lens (closed circles). For the 50 mm lens the

correlation between user-selected shifts and those determined by the automated algorithm are $r^2 = 0.94$ for horizontal movements and $r^2 = 0.93$ for vertical. Over the 40 images tested, the average of the standard deviation of the 10 user-selected positions was 0.34 pixels in the horizontal (azimuth) and 0.45 pixels in the vertical (tilt). The corresponding ranges of image movements are 2.0 pixels and 12.3 pixels respectively (as determined by the automated algorithm). In contrast, the average standard deviation of user-selected locations for the 12 mm lens images were considerably larger (1.29 pixels horizontal; 0.89 pixels vertical), while the ranges of movement were much smaller (1.7 pixels and 1.9 pixels respectively as determined by the automated algorithm). While the correlations between user-selected image shifts and calculated movements for the 12 mm lens were low ($r^2 = 0.16$ horizontal; $r^2 = 0.06$ vertical), we do not feel this necessarily indicates a failure of the auto-geometry algorithm. Rather, the large standard deviation within user-selected positions compared to the automatically detected range of movement suggests that the inconsistency of the users may be the dominant cause of the poor r^2 correlation when image movements are small.

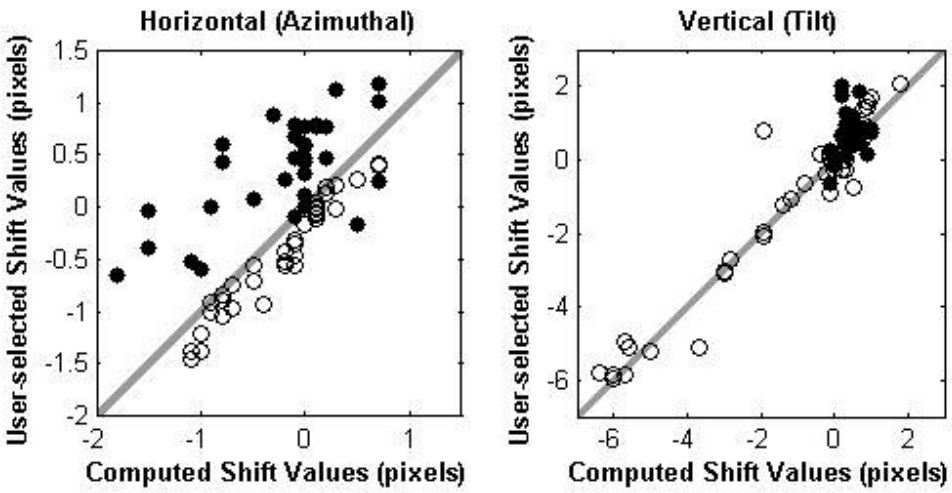

Figure 3.2. The computed image movement (the inverse of the camera movement) measured in pixels, plotted against the mean of 10 user-chosen movements from the same images. Open circles are from the 50 mm lens. Filled circles are from the 12 mm lens. The solid gray line is a one-to-one line representing perfect correspondence.

3.3. Shoreline Quantification

Once the lens distortion and camera movement have been corrected and the merged planform timex and variance images have been created, shorelines for each hour are extracted. It should be mentioned that numerous definitions of the shoreline exist ranging from the edge of a seaside cliff down to the toe of the beach (Boak and Turner, 2005). In this study we define the shoreline as the point visible in the timex where the image changes from what appears to be wet sand to time-averaged white swash (see Figure 3.1B). This definition of the shoreline is obviously tidally dependent, so the effects of tidal position must be taken into account in subsequent analysis. Clearly the suitability of this definition is subject to discussion, however for analyses of variation the exact

definition is not crucial so long as the identification procedures remain unchanged through time. The efforts of previous investigators, and our own, to repeatably extract the coordinates of the shoreline are described below.

One of the first methods to extract shorelines from imagery, shoreline intensity maximum method (SLIM; Plant and Holman, 1997), isolates the brightness peak in the timex due to wave breaking and swash motions. A second method focuses on intrinsic differences between the way light is reflected by wet and dry surfaces (Turner and Leyden, 2000). They found that the relative intensities of red and blue light in an RGB image diverge near the shoreline. For a specific site and lighting conditions a cutoff value can be chosen such that the shoreline could be determined for each column of pixels in the merged planform image as the division between the "whiter" beach and the "bluer" water. Another technique (Aarninkhof, 2003) found that casting the merged planform image from RGB into hue-saturation-value (HSV) space made it possible to isolate wet pixels from dry pixels using the ratio of hue and saturation values. Yet another technique relies on an artificial neural network (ANN) approach to isolate wet and dry pixels and hence the shoreline as the region between them (Kingston, in press). ANN requires the use of a training data set of manually identified wet and dry pixels and uses their characteristics to determine the state of pixels of unknown condition.

In this study, we seek a methodology that is transparent, robust and can run on hourly imagery with no user intervention. We investigated several of the procedures described above but found difficulty with those attempted. For instance, attempts to implement the

Aarninkhof (2003) procedure failed to produce clear groupings of pixels into wet vs. dry. The method of Turner and Leyden (2000) was quite reliable in certain lighting conditions, but lacked consistency in conditions of variable cloud cover and scene illumination, or when nearshore waters became so laden with sediment that their apparent color changed significantly. Over daily and longer time periods, it was found that threshold values between red and blue color fractions varied significantly requiring user intervention or additional algorithms in an attempt to produce dynamic thresholds. Thus, the shoreline methodology used in this study followed the SLIM approach, modified in an effort to improve its accuracy and robustness.

Previous attempts to isolate shorelines relied on *either* the timex or variance images. At Rehoboth Beach we find that neither alone is adequate due to variability in solar intensity, fog, color contrast between specific camera/lens pairs and beach usage requiring the use of both the timex and variance imagery to help isolate the shoreline in an automated sense. The timex image tends to fail on small wave days, when the timex pixel intensity peak in the surf zone can fall to the levels of other signals on the beach (e.g. the beach itself could appear brighter than the time averaged surf zone). In contrast, on large wave days variance images tend to display two regions of high pixel intensity, one at the outer edge of the surf zone where blue water alternates with white foam to produce variance, and another in the swash zone where white foam alternates with dark colored wet sand. Between these two lies an area of nearly continuously foam-covered water where the variance is very small. As wave heights diminish, the separation between these two alongshore bands of variance likewise falls and they eventually merge

into a single band of variance on small wave days. These differences cause difficulty in developing a single algorithm for shoreline identification from one image type.

To reliably identify shorelines in the broadest possible range of lighting conditions, sea states and patterns of beach use, a new image, referred to as the 'product image' is created (Figure 3.3B). The product image is calculated as the weighted average of the grayscale signal value of the timex (Figure 3.1B) and the grayscale signal value of the variance image pixel intensities (Figure 3.3A). The weighting was optimized experimentally to two thirds timex and one third variance. With more weighting towards the timex image the results became highly susceptible to changes in brightness, while weighting the variance more heavily made the results highly subject to errors associated with changing wave climates. The combination of both image types emphasizes regions where pixel intensity is both high and highly variable. To further enhance the image, (1) high frequency clutter is removed using a 2D 8 x 8 pixel low pass filter, (2) a mask delineating the possible search region for shorelines is applied, and (3) image pixel intensities are adjusted by a column-wise intensity stretch wherein only values above an adjustable threshold are preserved. The threshold value for the intensity stretch is determined as the greatest of: a) the signal value at the seaward edge of the mask, b) the signal value at the shoreward edge of the mask and c) 40% of the maximum signal value of that column within the mask. Signal values above this threshold are preserved and are adjusted to fill the full range of possible intensity values (Figure 3.3C).

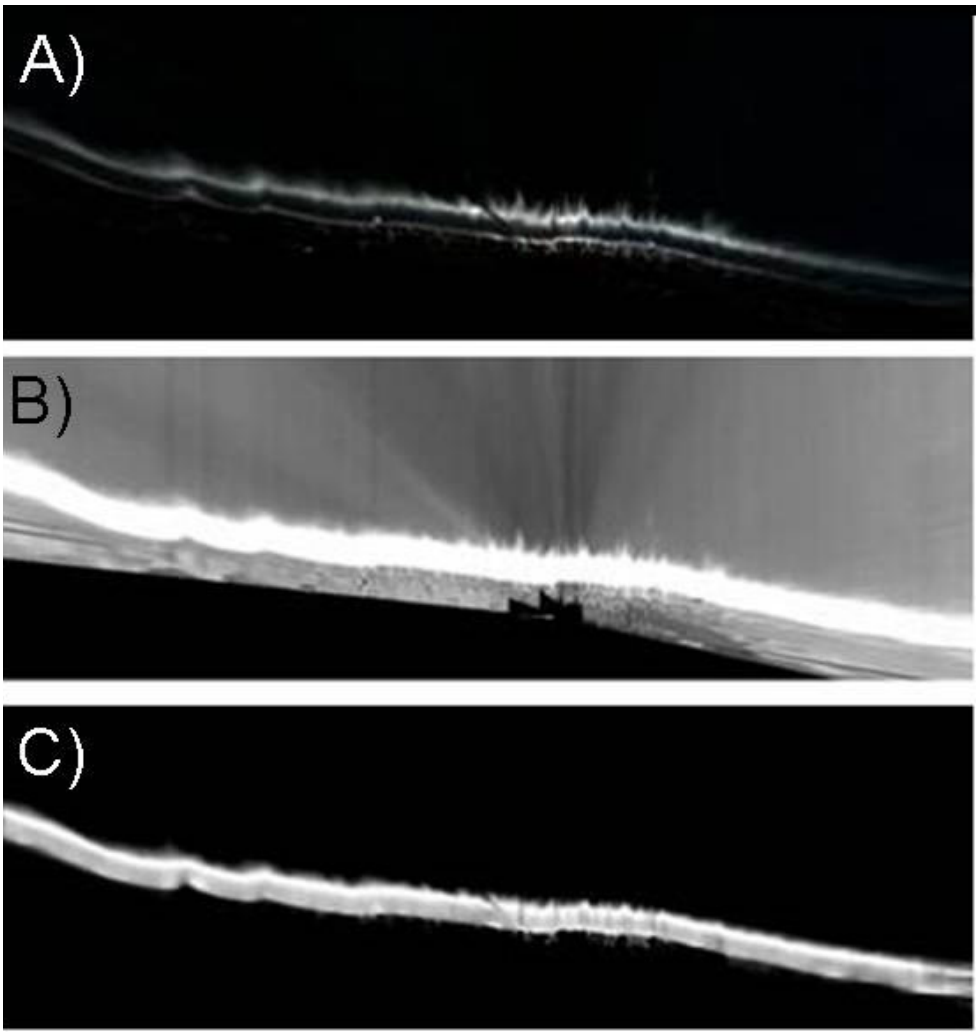

Figure 3.3. The image manipulation sequence prior to finding shorelines combines the variance image (A) with the timex image (Figure 3.1B) leading to the product image (B). (C) The product image is smoothed with a 2D low pass filter to reduce signal noise. An image mask is applied to isolate the region of interest, and a column-wise intensity stretch increases the signal to noise ratio of the surf zone.

Similar to the original SLIM method, the modified SLIM method operates on each column of the product image. Figure 3.4 shows an example of a pixel intensity spatial series. For reference, the merged planform timex in the vicinity of the selected cross-shore line is displayed as the upper subplot and the corresponding section of the product image is displayed as the lower subplot. In both subplots the solid line indicates the selected cross-shore line while the dashed lines indicate the bounds of the masked search region. The increase in intensity near 115 m is the outer edge of the surf zone. The shoreline is found as follows: (1) the peak intensity value within the surf zone is located, (2) a baseline intensity value is obtained as the average of the pixel intensities landward of the peak, (3) the cross-shore position where the intensity landward of the peak drops below the baseline is deemed the shoreline. The chosen cross-shore position of the shoreline is indicated in all three panels by an asterisk.

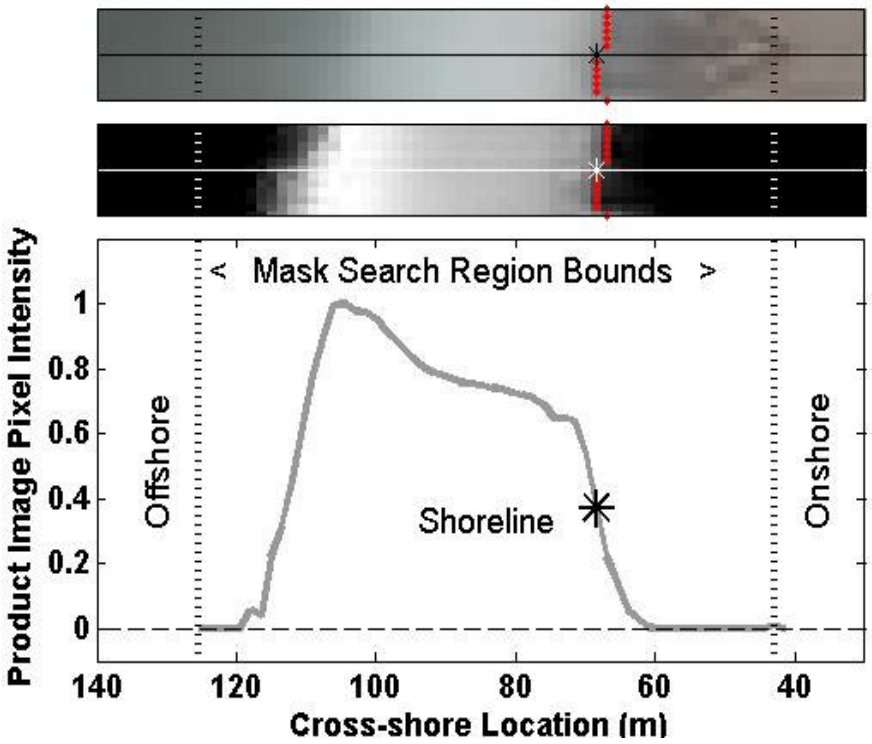

Figure 3.4. Example of surf zone pixel intensity from a single column in the product image. The subplots show a section of the merged timex image (top) and the same section of the resultant product image (middle) in the vicinity of the column where the pixel series was extracted (solid line in each). The calculated shoreline (red dots) and the bounds of the mask search region (dashed line) are also indicated. The shoreline is found independently for each column by tracking landward from the signal profile maximum to the point where the signal drops below the local signal average.

Repeating this procedure for each column of a product image derived from Figure 2.9 and the corresponding variance image, and plotting the resulting shoreline point in red produces the result found in Figure 3.5.

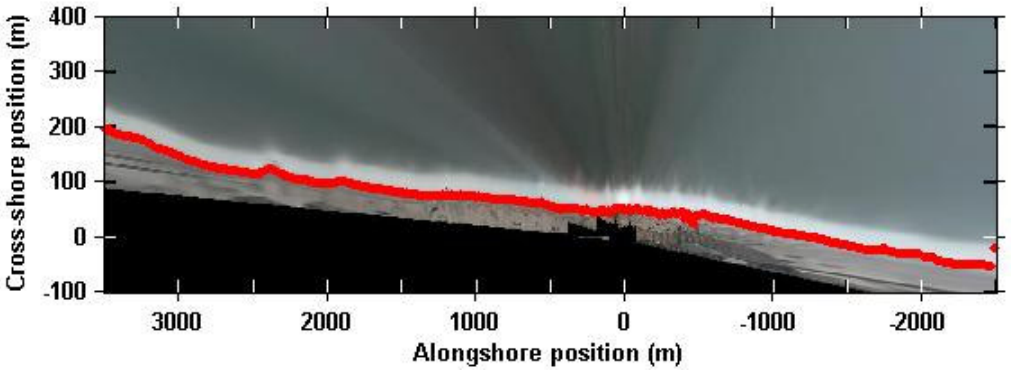

Figure 3.5: In each hour's shoreline data the shoreline position is found independently for each column of the product image.

3.4. Shoreline Picker Validation

Spatially dense and expansive shoreline data is needed to validate the modified SLIM procedure. Ideally, the shoreline would be mapped using a high resolution global positioning system, but that would require the surveyor to visually identify the mean shoreline and be able to sample large expanses of shoreline in less than one hour. Instead, we chose to validate the modified SLIM method against shoreline locations selected from timex images by eye. Six test images (Figure 3.8) with variations in wave height, light intensity and visibility were selected for validation. Ten users selected what they considered to be the shoreline at 20 equally spaced alongshore locations in each image (for a total of 120 different shoreline locations per user). Comparisons between the user-selected shorelines and those extracted via the modified SLIM procedure

indicate r^2 correlation coefficients ranging from 0.92 to 0.99 (Figure 3.7). The highest correlations are obtained from images taken on slightly overcast days where the surface illumination is less directional and glare is reduced (Figure 3.7A, 3.7E). The poorest correlations result from fog and poor visibility conditions where shoreline identification is difficult as evidenced by the large standard deviation in user-defined locations (Figure 3.7F). Based on this statistical analysis we believe the modified SLIM approach is robust. The six merged planform shoreline images in this analysis are provided in Figure 3.7. Note in Figure 3.7F cameras 1 and 2 are misaligned causing incomplete coverage of the shoreline a small distance south of the cameras.

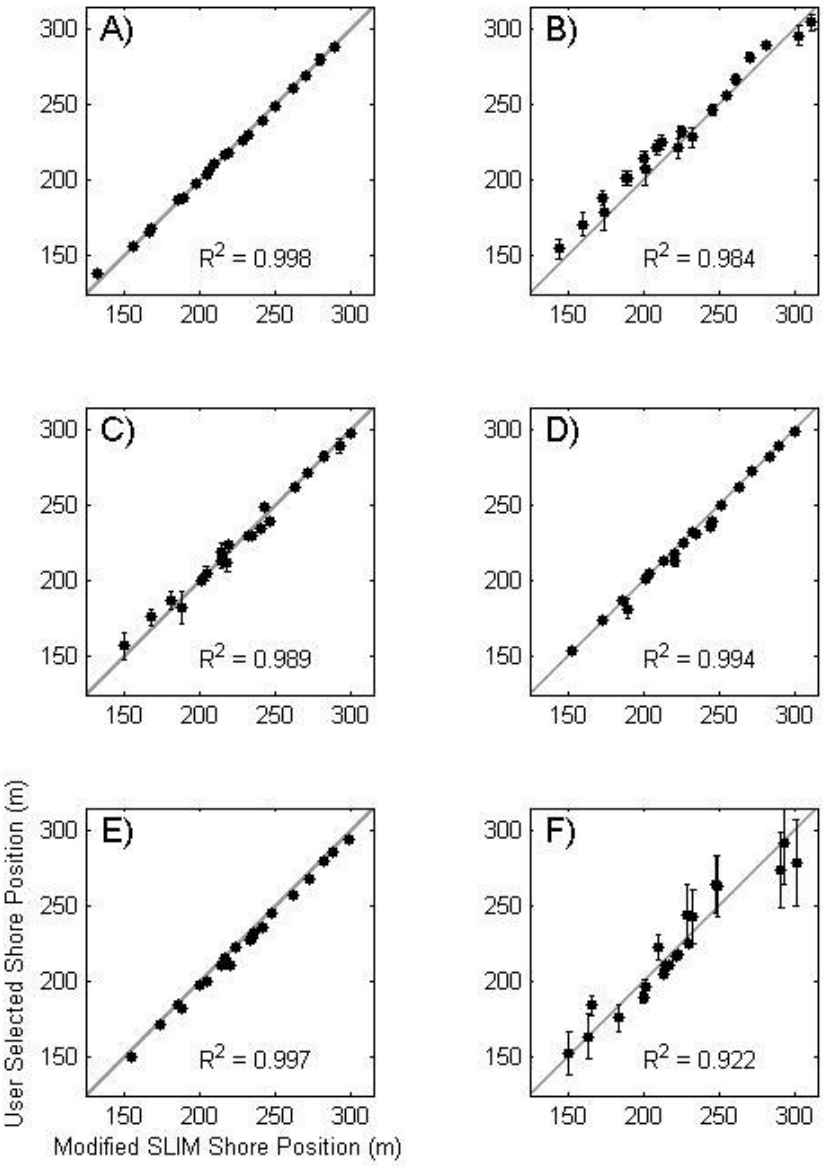

Figure 3.6. Regression analysis of computed cross-shore location of shoreline to mean user-selected shoreline for each of six images with different light and wave conditions. Error bars are 1 standard deviation either side of the mean. Solid gray line indicates one-to-one correspondence. The lighting and wave conditions assessed by each of these tests can be seen in Figure 3.7.

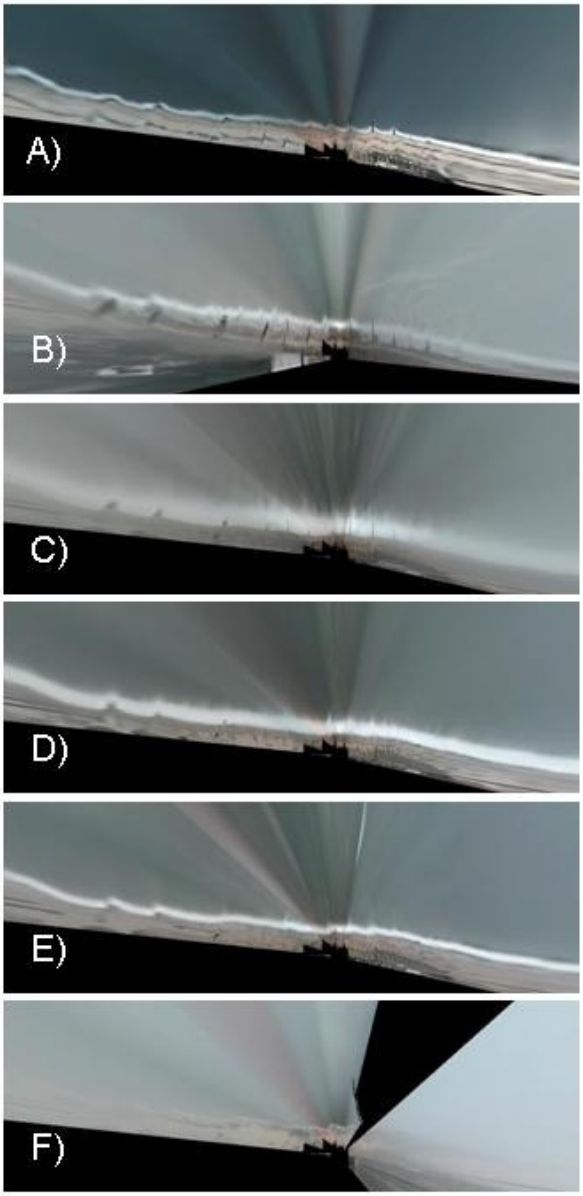

Figure 3.7: The images used for validation of the shoreline finding routine cover an array of lighting and wave conditions. A) Bright light, good visibility and moderate wave height. B) Flat light and good visibility due to high clouds, moderate wave height. C) Flat light with poor visibility and large wave height. D) Flat light with poor visibility and moderate wave height. E) Flat light with good visibility and low wave height. F) Bright light but poor visibility due to a low fog, low wave height.

Chapter 4

DATA VETTING & QUALITY CONTROL

Since images are collected every hour from 7 am to 6 pm regardless of weather conditions, inevitably some of the imagery will be of poor quality and produce incorrect extracted shorelines. Thus, to avoid user intervention in the shoreline identification process, quality control procedures are required. The abundance of data permits conservative safeguards to be implemented without severe reduction in temporal sampling density. The three parameters are used to cull data are shoreline quality, and small and large wave heights.

4.1 Computed Shoreline Quality:

Shorelines from product images tend to be fairly smooth in the alongshore direction. However, because the shoreline signal threshold is determined for each column of the product image independently, alongshore jump discontinuities in shoreline position will occur. It is assumed that large or frequent shoreline discontinuities are indicative of poor quality imagery and/or inaccurate shorelines, and subjective observations of shorelines corroborate this assumption. The first automated data discrimination is a quality parameter Q, defined as the inverse of the mean absolute value of alongshore shoreline gradient

$$Q = \left[\frac{1}{N-1} \sum_{n=2}^{N} \left| \frac{y_n - y_{n-1}}{x_n - x_{n-1}} \right| \right]^{-1}, \qquad (3)$$

where N is the number of alongshore locations. Large values of Q indicate a "smooth" shoreline, while small values of Q, indicate a jagged shoreline with large or frequent discontinuities. From numerous observations under various image qualities, a conservative value of $Q = 0.5$ was chosen as a cutoff for excluding shorelines. For this Q value, one-third of the shoreline data is rejected. As a reference, the Q value for the shoreline in Figure 3.5 is 2.52, exhibiting only some discontinuities around Yc = -400 m and a single anomalous point at Yc = -2500 m.

4.2 Small Wave Height:

When waves are small, shoreline pixel intensities in the variance and timex are low. By investigating numerous shorelines on days with small wave heights, we found an offshore wave height (NDBC buoy 40099) cutoff of 0.5 m was appropriate to reject shorelines that were often obviously incorrect. It is important to note that this parameter, along with large wave height, can only be implemented in a near real-time fashion if near real-time wave data is available, otherwise these constraints must be assessed from an archival wave height record in a post-processing step.

4.3 Large Wave Height:

When wave heights are large, wave setup can introduce errors relating to the presumed vertical elevation of the shoreline (Longuet-Higgins and Stewart, 1963, 1964). One empirical formulation for estimating wave setup is (Holman and Sallenger, 1985)

$$\overline{\eta}_{MAX} = 0.18 g^{1/2} S H_{\infty}^{1/2} T \,, \tag{4}$$

where $\overline{\eta}_{MAX}$ is the maximum wave setup at the shoreline, g is the acceleration due to gravity, S is the beach slope, H_{∞} is the deep water significant wave height and T is significant wave period. Since the cross-shore shoreline location error, E_{MAX}, is the projection of $\overline{\eta}_{MAX}$ onto the beach, it can be estimated as $\overline{\eta}_{MAX}$ divided by S

$$E_{MAX} = 0.18 g^{1/2} H_{\infty}^{1/2} T \,. \tag{5}$$

As an example, for an offshore wave height of 1.3 m and a typical period of 7 s, E_{MAX} would be 4.5 m, while for an offshore wave height of 0.5 m and the same wave period, E_{MAX} would be 2.8 m. Knowing instantaneous nearshore wave height information, errors due to wave setup can be reduced (e.g. Plant et al., 2007) but automated wave height determination from single camera imagery is difficult. Other formulations exist for estimating wave setup (e.g. Guza and Thornton, 1981) and yield similar estimates for E_{MAX}. The one given here is meant to be representative and to provide an upper error bound. In reality we expect setup errors to be much smaller because the surf zone width at Rehoboth Beach tends to be much narrower than the surf zone width at Duck, NC

where data to arrive at (5) were collected. Nonetheless, shorelines produced when the offshore wave height at NDBC buoy 40099 exceed a 1.3 m threshold were disqualified from consideration. These restrictions on wave height are similar to those previously used to improve data quality in video shoreline analysis (e.g. Turner and Leyden, 2000).

Approximately one-third of the all summer shorelines and half of the winter shoreline (see Chapter 5.1 for seasonal data definitions) fall outside the 0.5 – 1.3 m wave height window. Overlap between Q and the acceptable wave height envelope result in the elimination of approximately two-thirds of shoreline records, leaving an average of ~3.5 shorelines per day. Taking the wave setup and the cross-shore pixel resolution (Figure 2.5) we estimate a maximum horizontal shoreline positional error on the order of 5 m, comparable to previous video based shoreline studies (e.g. Elko et al., 2005). In reality, we believe the positional error in the majority of wave conditions is likely to be limited by the cross-shore pixel resolution (<2 m) given A) the narrow surf zone conditions at Rehoboth Beach and B) local beach wave heights often being significantly smaller than conditions at the offshore buoy due to propagation across the shelf and sheltering due to New Jersey.

4.4 Tidal Compensation

Figure 4.1 shows a one week time series of shoreline position from a single alongshore location as calculated by the modified SLIM method. The data gaps correspond to night time hours when no imagery is recorded. The dominant variability evident over the course of each day is that associated with tide level fluctuations, which can be seen to cause daily shoreline position variations on the order of 15 m.

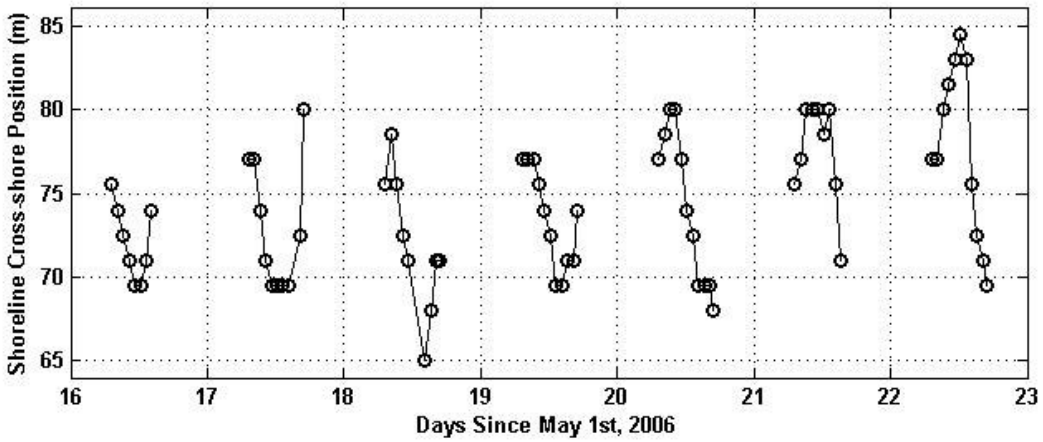

Figure 4.1. A one-week time series of shoreline position from a single alongshore location. Gaps in the time series are produced at night when no data collection occurs.

While shorelines at varying tide levels may provide topographic information (e.g. Plant and Holman, 1997; Aarninkhof and Roelvink, 1999), here we reduce the data to yield a daily–averaged shoreline. The dataset is divided into 14 subsets that are grouped according to a particular tide level with a range of ±0.05 m about that level. At Rehoboth Beach, these tidal sets range from 0.5 m below the tidal vertical datum to 0.8 m above it.

Assuming a 1:15 intertidal slope (a typical value for beaches in this area, Bosma and Dalrymple, 1997, and consistent with a 1 m tidal range and the ~15 m shoreline fluctuation seen in Figure 4.1), the estimated cross-shore error in shoreline position is ± 0.75 m.

To compare shoreline datasets at different tide levels, the data must be normalized. Normalization is accomplished by what is termed the "Mean Shoreline" approach, which is to subtract the mean shoreline from each tide-specific subset of data. Using this method, each individual normalized shoreline represents a departure from the mean at that tide, so that the difference between any two shorelines represents the change in cross-shore position over time. The Mean Shoreline approach emphasizes area where shoreline change is large. Using this methodology requires that shoreline cross-shore position change is not a function of tide level (vertical elevation), i.e. we assume there is a constant intertidal beach slope.

Before the 14 normalized shoreline change datasets are averaged together, the data are de-spiked. At every location (Day_i, Y_j) in the dataset there are N values of relative shoreline position, where N may be as many as 10 (one for each hour's data) distributed among the 14 possible tidal levels. To de-spike the data, the mean and standard deviation of those N values are computed (N_{MEAN}, N_{STD}). Any shoreline change values within that spacio-temporal location (Day_i, Y_j) that are more than 1 x N_{STD} away from N_{MEAN} are discarded from the dataset. This removes the data most likely to be erroneous.

Chapter 5

DATA ANALYSIS

Presenting a dataset that is more than a year long and consisting of 1001 alongshore position measurements in a meaningful way is a challenge. In order to graph the results of this study without discarding any of the information that was deemed to be of acceptable quality, a timestack was constructed. Within the timestack each row of data represents the relative cross shore position for that day. The magnitude of the change is indicated by the colorscale. Cold colors indicate erosion – a shoreline further shoreward than the average position, while hot colors indicate relative accretion.

5.1 Spatio-temporal Shoreline Variability

The timestack (Figure 5.1; center column) indicates spatio-temporal shoreline variability measured at the Rehoboth Beach study site between April 27, 2006 and October 1, 2007. The total dataset is artificially interrupted by a data gap of roughly three months (September 15, 2006 – December 19, 2006) caused by the removal of the cameras during reconstruction of the hotel rooftop following damage incurred by the landfall of tropical storm Ernesto on September 1st and 2nd, 2006. This large data gap can be seen in the timestack in Figure 5.1 as the horizontal band without color. The camera misalignment seen in Figure 3.8F persisted sufficiently along to skew the average results at that

alongshore position. Removal of those skewed data produced another band without color, oriented vertically, near alongshore position Yc = -150 m.

At the bottom of the central column of Figure 5.1 is a representative merged timex image intended to serve as a visual benchmark for the alongshore locations of the groins, the camera position, and other persistent features affecting alongshore variability. In the left and right columns are the corresponding offshore peak wave periods and wave heights respectively, recorded by NOAA-NDBC Buoy 40099. In the right hand plot the daily average of hourly wave data collected at the buoy is presented (black), along with the wave height envelope used to reduce setup errors (gray). Note that while the wave heights in the right-hand plot in Figure 5.1 are of daily averages, it is instantaneous hourly wave information which is used to cull shoreline data. It is therefore possible that data exists for days when the daily average wave height is outside of the allowable wave height envelope, and that not all hours are necessarily used when the daily average is within the envelope.

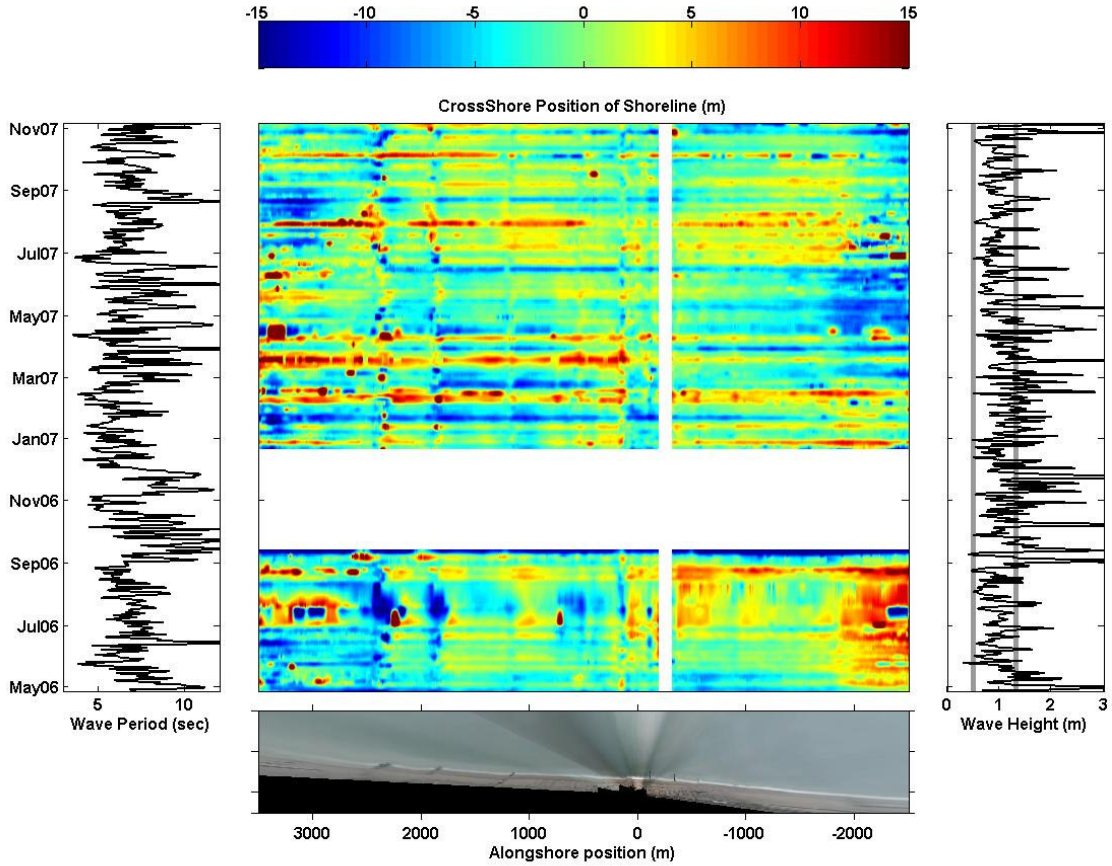

Figure 5.1. The shoreline time stack indicates daily shoreline records relative to the average shoreline for the span of the study (April 27, 2006 – November 5, 2007). Colors depict changes in cross-shore shoreline location at a given alongshore location (the abscissa) and at a given time (the ordinate). The area near alongshore position -150 m is removed due to camera misalignment, while data from fall 2006 is missing due to the hotel roof being repaired. Corresponding significant wave period and height from an offshore buoy are shown on the left and right respectively. The envelope of wave heights used in the study is marked in gray on the wave height record. A representative rectified timex is provided for positional reference at the bottom of the figure.

The most striking features in the timestack of Figure 5.1 are the strong vertical and horizontal regions of sediment accretion and erosion. Vertical bands indicate persistent shoreline features associated with dramatic changes in the shoreline profile. These are generally located near groins, the two most dramatic of which can be seen on the left of the timestack (at alongshore positions of roughly Yc = 1900 m and Yc = 2300 m). It is clear that the groins' effect on the shoreline is not constant over time. Instead, there is a distinct aperiodic oscillation of material deposition on the north and south sides of the groins as the sediment transport direction follows changes in the wave conditions on a 1-3 day climatological event timescale (e.g. Yankovsky and Garvine, 1997).

Horizontal features in the plot may be inferred to represent episodes of accretive or erosive conditions affecting the whole beach in a quasi-uniform manner. Examples of this kind of accretive event can be seen in late August 2006, in mid February, mid March and late July 2007. Generally, accretion is associated with conditions of long wave period and low wave heights, while large wave heights and shorter period waves are associated with erosion. By inspection, the August 2006, February 2007 and July 2007 accretive events in Figure 5.1 correspond to these generalizations, and the erosion following the February accretion event coincides with a period of large wave heights around Feb 14th, 2007. However, the accretive event in the middle of March 2007 seems to be associated with a large wave event.

5.2 Seasonal Shoreline Variability

Since differences exist between characteristic summer and winter weather patterns and climatological conditions along the Delaware coast, it is reasonable to reduce the complexity of the information in Figure 5.1 by examining typical summer and winter shoreline variability (Figure 5.2). The gap in data in the fall of 2006, though artificial, succeeds in dividing the data into subsets that may be used to represent typical summer and winter shorelines. To extend this analysis, the data is clipped at dates inferred to correspond to seasonal variations. The initial time-span extends from May 1, 2006 through August 31, 2006 and is termed "Summer 2006". A second time span extends from Dec. 19, 2006 through March 31, 2007 and is termed "Winter 2007". The final subset consists of shorelines dating from May 1, 2007 through August 31, 2007 and is likewise termed "Summer 2007". The month of April, both in 2006 and in 2007, along with data from after September 1, 2007 are removed from this analysis in order to satisfy the desire to have summer and winter data sets consisting of similar length and to exclude some span of time in which climatological conditions are less likely to be uniformly representative of characteristic seasonal norms.

Figure 5.2A shows the average shorelines, relative to the global mean, for each of the three time periods as a function of alongshore position. The approximate location of groins is indicated by the dashed lines. The alongshore extent of the groins increases with distance from the cameras as the projection of their vertical profile is smeared onto the tidal level. Perhaps the most important information in Figure 5.2A is indication of areas of greater or lesser erosion, which by inspection is largely controlled by groin

locations. For instance, at the groins located at Yc = 1100 and Yc = 1900 the average summer shoreline south of the groins extend further seaward than it does in the winter by up to 6 m. Another observation is that in the groin cell immediately in front of the cameras the average shoreline in both summer periods is significantly advanced from the winter average while in the next groin cell northward the opposite is true.

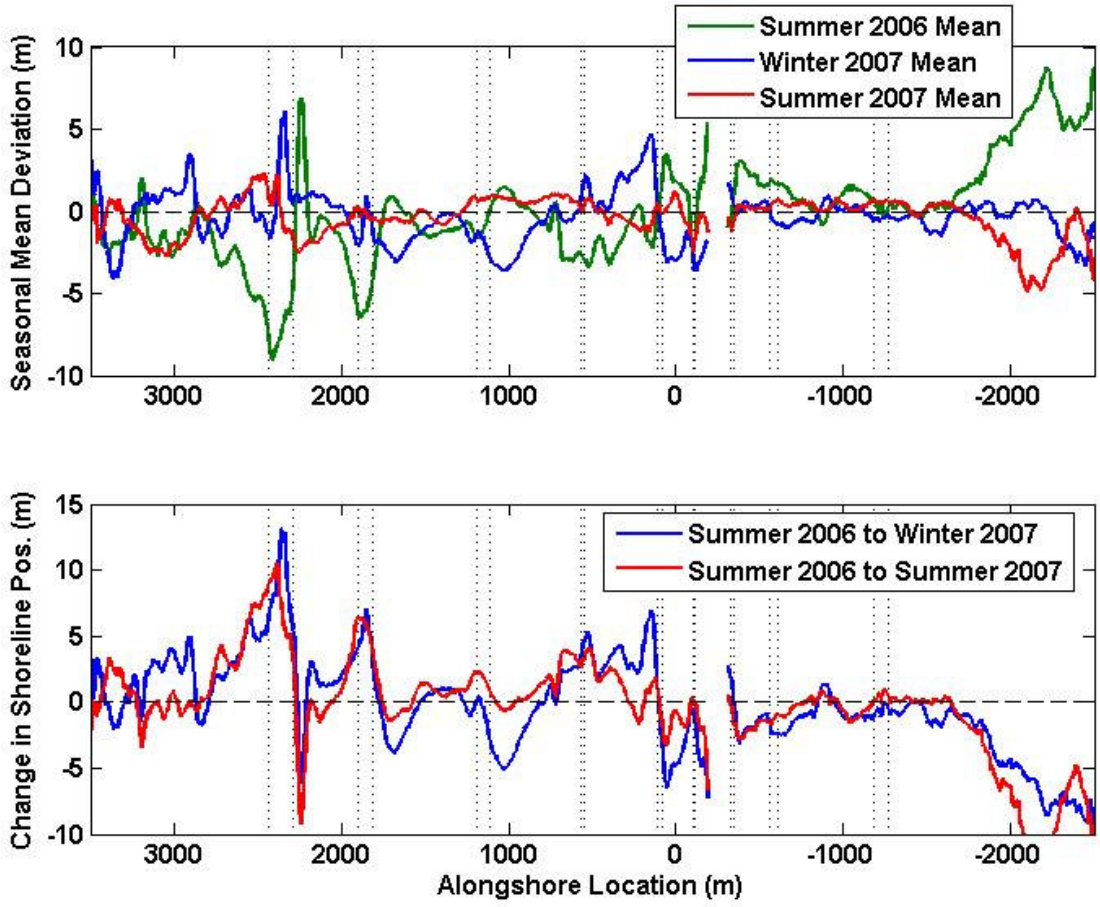

Figure 5.2. Comparisons of summer 2006 (5/1/06 - 9/2/06) winter 2007 (12/19/06 – 3/31/07), and summer 2007 (5/1/07 - 9/2/07)and mean shoreline. A) The seasonal mean shorelines are normalized by the global average shoreline. Total shoreline position change (B) can be assessed as the difference between the initial (2006) mean summer shoreline and each of the two subsequent mean seasonal shorelines. Change from summer 2006 to summer 2007 indicate a mean seasonal shoreline recession of 0.3 m.

To more directly assess the change between the mean summer and winter shoreline positions, the seasonal difference is presented in Figure 5.2B. Average seasonal shoreline change from Figure 5.2B is -0.3 m, lower than, but consistent with typical estimates along the coast (Garriga and Dalrymple, 2002). While this 0.3 m average shoreline recession is significantly smaller than the previously estimated maximum shoreline position error of 5 m, the 0.3 m value is derived from seasonal averages of roughly 100 days each, which we expect to be free from systemic seasonal bias. Also of great interest is the alongshore variability. North of the cameras the average shoreline change between Summer 2006 and Summer 2007 is an accretion of 1.3 m, while south of the cameras there is on average 2.8 m of erosion. This inhomogeneity and the area of dramatically increased erosion in both the Winter and Summer 2007 mean shorelines south of Yc = -1750 m may be due to the decay of the summer 2005 beach nourishment discussed in Chapter 1.3. The construction of the groin at Herring Point (labeled in Figure 1.1D), which we hypothesize will cause measurable shoreline advance in the northern edge of the study site could also have contributed to the net accretion found in the northern part of the study site.

Another exception to the general trend of shoreline recession is evident in the area between about Yc = 200 m to Yc = 800 m. We speculate that accretion in this area may have resulted from the erosion of a man-made dune foot built further seaward than the rest of the reconstructed dune (visible in the camera 5 and camera 6 images of Figure 2.7). Additional sediment was supplied to this area by DNREC after several storm events during the winter of 2007 to protect an area of surface street threatened by erosion.

Chapter 6

DISCUSSION

In this study we describe the development of an automated system for video derived analysis of shoreline variability. The analysis at Rehoboth Beach, Delaware revealed trends in seasonally averaged shoreline variability with magnitudes of ~ 10 m and alongshore variations closely associated with the locations of shore-normal groins. Between the summer periods of 2006 and 2007 seasonally averaged shorelines indicate and average erosion of 0.3 m. In this chapter the relationship between this shoreline recession and volumetric change of beach sediment remain to be examined, possible errors in the assumed vertical rectification plane will be discussed, and possible factors affecting the movement of the cameras will be analyzed.

6.1 Beach Planform Area and Volume

Beach planform area has been used previously as a proxy for the alongshore distribution of sediment volume (Norcross et al., 2002; Miller and Fletcher, 2003; Farris and List, 2007), and hence may be a useful measure in the quantification of beach change and volumetric beach nourishment evolution. By assuming an equilibrium beach profile (EBP), changes in shoreline position and sediment volume can be related by the Bruun Rule (Bruun, 1962)

$$\Delta V = \Delta y(h^* + b)L, \quad (6)$$

where V is sediment volume, y is the cross-shore position of the shoreline, b is the berm height, h^* is the maximum depth of the active profile and L is the alongshore extent of the area in question. In a previous study of this area, Garriga and Dalrymple (2002) used values of b = 2.13 m and h^* = 7.31 m.

To assess the accuracy of Equation 6 requires accurate sediment volume measurements. This study was conducted in parallel with another study using terrestrial LIDAR surveys over a 500 m stretch of this beach (Pietro et al., accepted). Between surveys conducted in late April, 2006 and Jan 31st, 2007 they found a total sediment volume loss of 11,544 m^3. Over the same 500 m alongshore span and the same time interval the video derived shoreline change was found to be -3.8 m. Through the use of Equation 6, a 3.8 m shoreline retreat corresponds to an estimated volumetric loss of 17,936 m^3; an overestimate of 55 %. For this 500 m section, Pietro et al., (accepted) showed that comparisons between LIDAR-derived monthly area and volume did not covary (r^2 = 0.43) and the volumetric overestimate using video-derived shoreline data suggests beach planform cannot be used as a proxy for beach volume at this location.

Relationships between beach area and volume were not found at Rehoboth beach, but have been successfully parameterized at other sites (e.g. Farris and List (2007) found r^2 values between the two parameters ranging from 0.71 to 0.96). While we did not directly

investigate the validity of the cited h^* and b, we note that to equate the video-derived volumetric loss (based on Equation 6) with LIDAR-derived volumetric loss (Pietro et al., accepted) requires reducing the quantity ($h^* + b$) by 36%. It must be noted that this decrease would not improve the correlation coefficient between LIDAR-derived area and volume data. One possible explanation for the poor prediction of volumetric change is that factors associated with recreational beach use, including the effects of frequent grooming, an artificial dune line and occasional sediment redistribution by bulldozers may significantly affect the relationship between beach area and sediment volume. Another possible explanation is the reliance on an EBP, which may be an inappropriate assumption for shoreline response (Pilkey, 1993). If the EBP assumption is rejected, a simple relationship between area and volume is not expected. It must also be pointed out that the algorithm used for tidal averaging assumes an EBP exists at least in the intertidal zone, a much less restrictive requirement since the intertidal zone makes up only about 15% of the vertical domain of the beach profile. While the true cause of the low correspondence between beach area to volume cannot be ascertained, we suggest that the planform area should not be used as an indicator of volumetric nourishment performance at Rehoboth Beach.

6.2. Errors to the Vertical Elevation of the Rectification Plane

If the vertical position of the shoreline differs from the predicted tidal elevation used in image rectification, the plane onto which the images are rectified will be incorrect. At large distances from the cameras the alongshore positions of fixed objects will be highly inaccurate. Two principle factors may contribute to an incorrect assumed vertical

location of the merged image plane. One of these is wave setup (Chapter 4.3). Because of the wave height cutoffs used in this analysis, errors from this source are expected to be limited to between 0.19 m and 0.30 m vertically. The second is possible error in the calculated tide level based on tidal harmonics. Comparison of predicted tides with historical tidal records (Figure 7.1) at the tide gage in Ocean City, MD (~40 km south of the study site) indicate that tide estimation errors are usually less than 0.2 m. Severe storm surge may increase the error to over ~ 0.6 m, however it must be noted that periods of storm surge tend to coincide with large wave events, and data taken during such events are removed from analysis.

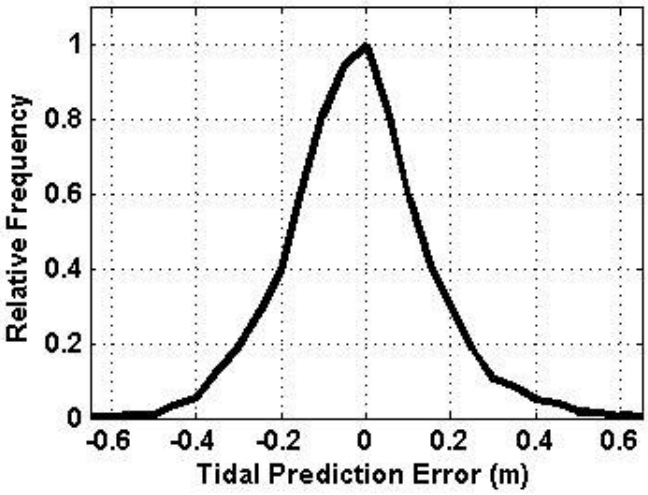

Figure 6.1: Histogram of tide level discrepancy (left) between predicted and measured sea surface elevation. This distribution represents 2 years of data recorded outside the surf zone at Ocean City, Maryland.

6.3 Camera Movement

Until recently (Holman and Stanley, 2007), subtle camera movements in fixed platform imagery for coastal applications were largely ignored. In this study, we were surprised to find large movements in the calculated positions of fixed objects. Movements were most readily apparent for the images obtained through the 50 mm lens where the rectified positions of fixed groins shifted considerably. For example, movements of the apparent location of the groin at Yc = 2300 m were as great as 500 m in the alongshore before geometrical correction. While movements were likely occurring for all cameras, the effects of this motion are most notable for the 50 mm lens for two reasons: (1) a 50 mm lens has a field of view of only 7°, so a small change in the tilt of the camera causes a significant change in image location and (2) the line of sight from the 50 mm lens to the shoreline it images is within 1° of horizontal, so small changes in image location are interpreted as large changes in real world coordinates.

The variations in tilt angle required to cause a 500 m shift in groin position can be determined as

$$CameraTilt = \arctan\left(\frac{CE}{DG}\right), \tag{7}$$

where CE is the camera elevation (roughly 30 m) and DG is the distance to the groin (2200 to 2700 m for the maximum observed apparent groin location change). The calculated tilt change of 0.14° (0.0025 radians) could be induced by one edge of the palette lifting relative to the other by only ~0.0003 m. To attribute a dimensional change

of this order to expansion and contraction of the wood of the palette, the rubber sheet of the roof, the insulation foam below the rubber roof sheet, and even the structure of the building itself seems reasonable.

While small movements were found with 24h periodicity similar to those found by Holman and Stanley (2007), attributable to daily fluctuations in temperature or insolation, camera movements with significantly larger magnitudes were also found with timescales of roughly one month. Efforts to find a correlation to any causal factor proved fruitless. The timescales of variation in rainfall and humidity are much smaller than those of the camera movement, while the timescales of seasonal temperature and insolation variation are much longer.

Chapter 7

SUMMARY AND CONCLUSIONS

Video imaging systems are an increasingly important tool for the quantification and evaluation of morphodynamics and nearshore processes. They have been developed to be highly effective in a variety of coastal conditions, and can provide data on a variety of timescales and measure a variety of parameters in near-real time. In areas like Delaware's Atlantic coast that depend on periodic beach nourishment for shoreline maintenance, near real-time assessment of shoreline position becomes not only a matter of scientific interest, but also one with important implications for coastal zone management.

In this study we present the development of tools for automated shoreline detection, as well as an analysis of a dataset at Rehoboth Beach, DE spanning roughly a year and a half. A methodology is described for correction of camera azimuthal and tilt movement derived from correlation techniques. Validation of this method against user interpretation of camera movement indicates r^2 correlation coefficients exceeding 0.9 when movement exceeded 1 pixel. Shorelines spanning 6 km of the coastline are automatically extracted from hourly imagery using a modified shoreline intensity maximum method (Plant & Holman, 1997) dependent on cross-shore variations in pixel intensity. Correlations

against user-selected shorelines have an r^2 value greater than 0.92 in a variety of hydrodynamic and lighting conditions.

Seasonally averaged shoreline variability indicates a trend of rapid accretional and erosional episodes, amplified in the vicinity groins to shoreline position changes of ~10 m. Seasonally averaged data indicate predominant accretion on the northern side of groins and erosion on the southern side during the winter months and the opposite during summer months in accordance with established patterns of seasonal net littoral sediment transport. Analysis of seasonal trends in shoreline change also suggest that the effects of the beach nourishment conducted in the summer of 2005 still exerted a significant influence on the cross-shore shoreline position in the southern section of the study site through the summer of 2006, though shoreline changes associated with the evolution of the nourishment were insignificant between the winter and summer of 2007. The net seasonal shoreline change indicated erosion of 0.3 m consistent with previous estimates for this region. Unlike previous studies at other sites, beach width derived from video imagery was found to be a poor predictor of beach volume.

REFERENCES

Aarninkhof, S. G. J., and J. A. Roelvink (1999), Argus-Based Monitoring of Intertidal Beach Morphodynamics, *Coastal Sediments, 99*, 2429-2444

Aarninkhof, S. G. J., and R. A. Holman (1999), Monitoring the nearshore with video, *Backscatter*, *10*, 8-11.

Aarninkhof, S. G. J. (2003). Nearshore Bathymetry Derived from Video Imagery. *Technical University of Delft, Delft*. 175pp.

Aarninkhof, S. G. J., I. L. Turner, T. D. T. Dronkers, M. Caljouw and L. Nipius (2003). A video technique for mapping intertidal beach bathymetry. *Coastal Eng., 49*, 275-289.

Adrian, R.J. (1991), Particle-imaging techniques for experimental fluid-mechanics, *Annual Review of Fluid Mechanics*, volume 23

Boak, E. H. and I. L. Turner (2005), Shoreline Definition and Detection: A Review, *J. Coastal Res., 21-4*, 688-703.

Bosma, K. F. and R. A. Dalrymple (1997), Beach Profile Analysis Along the Delaware Atlantic Coastline, *U. Del. Research Report, No. CARC-97-05*.

Bruun, P. (1962), Sea Level Rise as a Cause of Shore Erosion, *J. Waterway, Port, Coastal and Ocean Eng., ASCE, 88*, 117-130.

Chickadel, C. C., R. A. Holman, H. H. Freilich (2003), An optical technique for the measurement of longshore currents, *J. Geophys. Res.*, *108*.

Clausner, J. E., Gebert, J. A., Rambo, A. T. and Watson, K. D. (1991). Sand bypassing at Indian River, Delaware, *Proc. Coastal Sediments '91*, ASCE, 1177-1191.

Dalrymple, R. A. and D. W. Mann (1985), A Coastal Engineering Assessment of Fenwick Island, Delaware, *U. Delaware Ocean Eng. Tech. Report, No. CE-54*.

Davidson, M., M. van Koningsveld, A. de Kruif, J. Rawson, R. Holman, A. Lamberti, R. Medina, A. Kroon and S. Aarninkhof (2007), The CoastView project: Developing video-derived Coastal State Indicators in support of coastal zone management, *Coastal Engineering*.

Farris, A. S., and J. H. List (2007), Shoreline Change as a Proxy for Subaerial Beach Volume Change. *J. of Coastal Res., 23, 3*, 740-748.

Frasier, S. J., et al. (1995), Directional ocean wave measurements in a coastal setting using focused array imaging radar, *IEEE Trans. Geosci. Remote Sens.*, *33*, 428-440.

Garriga, C. M. and R. A. Dalrymple (2002), Development of a Long-Term Coastal Zone Management Plan for the Delaware Atlantic Coast, *U. Del. Research Report, No. CARC-02-04*.

Guza, R. T., and E. B. Thornton (1981). Wave set-up on a natural beach. *J. Geophys Res., 86 (C5)*, 4133-4137.

Hart, D. P. (1998), High-speed PIV analysis using compressed image correlation. *Journal of Fluids Engineering-Transactions of the ASME, 120, 3,* 463–470.

Holland, K. T. and R. A. Holman (1997), Video estimation of foreshore topography using trinocular stereo, *J. Coastal Res.*, *13*, 81-87.

Holland, K. T., R. A. Holman, T. C. Lippmann, J. Stanley and N. Plant (1997), Practical Use of Video Imagery in Nearshore Oceanographic Field Studies. *IEEE J. of Oceanic Eng., Vol13, No. 1,* 81-92.

Holland, K. T. (2001), Application of the Linear Dispersion Relation with Respect to Depth Inversion and Remotely Sensed Imagery, *IEEE Trans. Geosci. Remote Sens.*, *39*, 2060-2072.

Holland, K. T. and J. A. Puleo (2001), Variable swash motions associated with foreshore profile change, *J. Geophysical Res., 106-C3*, 4613–4624

Holland, K. T., J. A. Puleo and T. N. Kooney (2001), Quantification of swash flows using video-based particle image velocimetry, *Coastal Engineering*, *44*, 65-77.

Holman, R. A. and A. H. Sallenger (1985), Set-Up and Swash on a Natural Beach, *J. Geophysical Res., 90(C1)*, 945-953.

Holman, R. A. and J. Stanley (2007), The history and technical capabilities of Argus, *Coastal Engineering*.

Honeycutt, M. G. (2003), Spatial Variability in Shoreline Change along the Atlantic Coast of Delaware: Influences of the Geologic Framework, *Ph.D. Dissertation; U. Del. Col. Marine Studies, GC-9999 (2004), .H772 (2003).*

Karara H. M., and Y. I. Abdel-Aziz, (1974), Accuracy aspects of nonmetric imageries, *Photogramm. Eng. Remote Sens., vol 40*, 1107-1117

Kingston, K.S, C. Mallet, N. G. Plant and M. A. Davidson (in press), Inter-tidal mapping of morphological features from remotely sensed data. *Coastal Engineering*.

Lippmann, T. C., and R. A. Holman (1989), Quantification of sand bar morphology: A video technique based on wave dissipation, *J. Geophys. Res.*, *94*, 995-1011.

Lippmann, T. C., and R. A. Holman (1991), Phase speed and angle of breaking waves measured with video techniques, in *Coastal Sediments '91*, edited by N. C. Kraus, et al., pp. 542-556, ASCE, New York.

Longuet-Higgers, M. S. and R. W. Stewart (1963), A Note on Wave Set-Up, *J. Marine Research, 75*, 4-10.

Longuet-Higgers, M. S. and R. W. Stewart (1964), Radiation Stress in Water Waves, a Physical Discussion with Applications, *Deep-Sea Research, 11*, 529-563.

Madsen, A. J., and N. G. Plant (2001), Intertidal Beach slope predictions compared to field data, *Marine Geo., 173*, 121-139.

McNinch, J. E. (2007), Bar And Swash Imaging Radar (BASIR): a mobile X-band radar designed for mapping sand bars and swash-defined shorelines over large distances, *J. Coastal Res.*, *23*, 59-74.

Miller, T.L. and C.H. Fletcher (2003), Waikiki: Historical analysis of an engineered shoreline. *J. Coastal. Res.*, 19, 1026-1043.

Norcross, Z.M., C.H. Fletcher and M. Merrifield, (2002), Annual and interannual changes on a reef-fringed pocket beach: Kailua Bay, Hawaii, Marine Geology, 190, 553-580.

Pietro, L. S., M.A. O'Neal and J.A. Puleo (submitted), Developing terrestrial-lidar-based digital elevation models to assess beach nourishment performance at Rehoboth Beach, DE, *J. Coastal Res*.

Pilkey, O. H., R. S. Young, S. R. Riggs, A. W. Smith, H. Wu and W. D. Pilkey (1993), The concept of profile of equilibrium: A critical review, *J. Coastal Res., 9,* 255-278.

Plant, N. G. and R. A. Holman (1997), Intertidal beach profile estimation using video images, *Marine Geology*, 140, 1-24.

Plant, N. G., S. J. J. Aarninkhof, I. L. Turner, K. S. Kingston (2007), The performance of shoreline detection models applied to video imagery, *J. Coastal Res, 22, 3*, 657-670.

Puleo, J. A., G. Farquharson, S. J. Fraiser and K. T. Holland (2003), Comparison of optical and radar measurements of surf and swash zone velocity fields, *J. Geophys. Res.*, *108*, 45-41 - 45-12.

Robertson V. W., D. Whitman, K. Zhang and S. P. Leatherman (2004), Mapping Shoreline Position Using Airborne Laser Altimetry, *J. Coastal Res., 20-3*, 884-892.

Roth, G., D. Hart and J. Katz (1995) , Feasibility of using the L64720 video motion estimation processor (MEP) to increase efficiency of velocity map generation for particle image velocimetry (PIV). In: T.T. Huang, Editor, *ASME/JSME Fluids Engineering and Laser Anemometry Conference and Exhibition, American Society of Mechanical Engineers, Hilton Head, SC (1995)*, 387–393.

Stockdon, H. F., and R. A. Holman (2000), Estimation of wave phase speed and nearshore bathymetry from video imagery, *J. Geophys. Res.*, *105*, 22015-22033.

van Enckevort, I. M. J., and B. G. Ruessink (2001), Effect of hydrodynamics and bathymetry on video estimates of nearshore sandbar position, *J. Geophys. Res.*, *106*, 16969-16979.

Stockdon, H. F., A. H. Sallenger, J. H. List and R. A. Holman (2002). Estimation of shoreline position and change using airborne topographic lidar data. *J. Coastal Res., 18(3)*, 502-513.

Tsai, R. Y., (1987), A versatile camera calibration technique for high-accuracy 3D machine vision metrology using off-the-shelf TV cameras and lenses, *IEEE J. Robot. Automation, vol RA-3*, 323-344.

Turner, I, and V. Leyden, (2000), System Description and Analysis of shoreline Change: August 1999-February 2000. Report 1. Northern Gold Coast Coalsal Imaging System *(Technical Report 00/12). Sydney Australia: Water Research Laboratory, Univeristy of New South Wales.*

Turner, I. L., D. Whyte, B. G. Ruessink and R. Ranasinghe (2007), Observations of rip spacing, persistence and mobility at a long, straight coastline, *Marine Geology, 236*, 209-221.

U.S. Army Corps of Engineers (1997), A Report on the Storm Damage Reduction and Shoreline Protection Project for Rehoboth Beach and Dewey Beach, Delaware Pursuant to Section 101(b)(6) of the Water Resources Development Act, 1996, *U.S. Government Printing Office, 43-884*.

van Enckevort, I. M. J., and B. G. Ruessink (2001), Effect of hydrodynamics and bathymetry on video estimates of nearshore sandbar position, *J. Geophysical Res., vol 106-C8*, 16,969-16,979.

van Enckevort, I. M. J., and B. G. Ruessink (2003), Video observations of nearshore bar behavior. Part 1: alongshore uniform variability, *Continental Shelf Res., 23*, 501-512.

Yankovsky, A. E., and R. W. Garvine, 1998: Subinertial dynamics on the inner New Jersey shelf during the upwelling season. *Journal of Physical Oceanography, 28*, 2444-2458.